



Article

Climate Change and Vegetation Greening Jointly Promote the Increase in Evapotranspiration in the Jing River Basin

Luoyi Yao ^{1,2,†}, Rong Wu ^{3,†}, Zijun Wang ³, Tingyi Xue ², Yangyang Liu ^{1,2,4,*}, Ercha Hu ^{4,5,*}, Zhongming Wen ² , Haijing Shi ⁶ , Jiaqi Yang ², Peidong Han ², Yinghan Zhao ² and Jingyao Hu ²

¹ Key Laboratory of Coupling Process and Effect of Natural Resources Elements, Beijing 100055, China; yaolyxbl@nwafu.edu.cn

² College of Grassland Agriculture, Northwest A&F University, Xinong Road 22, Yangling 712100, China

³ College of Water Resources and Architectural Engineering, Northwest A&F University, Yangling 712100, China

⁴ Inner Mongolia Daqingshan Forest Ecosystem National Observation and Research Station, Inner Mongolia Academy of Forestry Sciences, Hohhot 010010, China

⁵ Inner Mongolia Academy of Forestry Sciences, Hohhot 010010, China

⁶ State Key Laboratory of Soil Erosion and Dryland Farming on Loess Plateau, Institute of Soil and Water Conservation, Northwest A&U University, Yangling 712100, China

* Correspondence: lyy19910728@nwafu.edu.cn (Y.L.); hec2000@emails.imau.edu.cn (E.H.)

† These authors contributed equally to this work.

Abstract: Within the Earth's terrestrial environment, evapotranspiration significantly contributes to the hydrological cycle, accounting for around 80% of the precipitation on landmasses to be reintroduced into the atmosphere. This mechanism profoundly affects the distribution and availability of surface water resources throughout the ecosystem. Gaining insight into the factors influencing local evapotranspiration fluctuations in response to varying climatic and vegetative scenarios is crucial for effective water management strategies and rehabilitating ecosystem resilience. To this end, our study focuses on the Jing River Basin in the Loess Plateau, utilizing multi-source remote sensing data and climatic information to investigate the spatiotemporal dynamics of evapotranspiration from 1984 to 2018 through the application of the Priestley–Taylor Jet Propulsion Laboratory (PT-JPL) model. Our research results indicate a general ascending tendency in evapotranspiration across the investigated region, demonstrating a notably discernible escalation at a pace of approximately 3.11 mm/year ($p < 0.01$), with an annual vegetation ET volume reaching 533.88 mm. Across different vegetation types in the Jing River Basin between 1984 and 2018, the mean yearly ET was observed to be highest in forests (572.88 mm), followed by croplands (564.74 mm), shrublands (536.43 mm), and grasslands (503.42 mm). The leaf area index (LAI) demonstrated the strongest partial correlation with ET ($r = 0.35$) and contributed the most significantly to the variation in ET within the Jing River Basin (0.41 mm/year). Additionally, LAI indirectly influences ET through its impact on vapor pressure deficit (VPD), precipitation (Pre), and temperature (Temp). Radiation is found to govern most ET changes across the region, while radiation and precipitation notably affected ET by modulating air temperature. In summary, these radiant energy changes directly affect the evaporation rate and total evapotranspiration of surface water. It provides important support for understanding how evapotranspiration in the Jing River Basin is adjusting to climate change and increased vegetation cover. These findings serve as a theoretical foundation for devising sustainable vegetation restoration strategies to optimize water resource utilization within the region.



Citation: Yao, L.; Wu, R.; Wang, Z.; Xue, T.; Liu, Y.; Hu, E.; Wen, Z.; Shi, H.; Yang, J.; Han, P.; et al. Climate Change and Vegetation Greening Jointly Promote the Increase in Evapotranspiration in the Jing River Basin. *Agronomy* **2024**, *14*, 1910. <https://doi.org/10.3390/agronomy14091910>

Academic Editor: Koffi Djaman

Received: 30 June 2024

Revised: 14 August 2024

Accepted: 19 August 2024

Published: 26 August 2024



Copyright: © 2024 by the authors. Licensee MDPI, Basel, Switzerland. This article is an open access article distributed under the terms and conditions of the Creative Commons Attribution (CC BY) license (<https://creativecommons.org/licenses/by/4.0/>).

Keywords: Jing River Basin; evapotranspiration; vegetation greening; climate change

1. Introduction

The fluctuations within the global climate system have exerted profound impacts on the overall functioning of our planet. Remarkably, over the past few decades, significant

climatic variations have affected the hydrological mechanisms of numerous river basins, encompassing critical meteorological elements. Water, as a vital natural resource, holds an irreplaceable position in sustaining life forms and fostering societal progress [1–3]. However, some scholars found that due to the limited water supply, the global trend of land evapotranspiration has recently decreased [4]. In response, China has formulated the technical code for the comprehensive control of soil and water loss in small watersheds, converting farmland to forest and grassland, and the ecological compensation system, including soil and water conservation farming techniques. The aim is to improve soil anti-erodibility, increase soil water content, reduce soil erosion, and increase crop yields by changing topography, increasing vegetation coverage, enhancing soil infiltration, and reducing soil evaporation [1]. On the Earth's surface, water resources are constantly exchanged with the atmosphere through precipitation, runoff, evapotranspiration, and infiltration. Evapotranspiration, in particular, is crucial to the global water cycle, influencing water availability. Evaporation is not only the physical transfer of water, it is the pulse of our Earth's hydrological system, maintaining the balance of the ecosystem [2,3]. It is very important to accurately assess the influence of meteorological conditions and plant life on water evaporation and movement to fully understand the changing law of water resource balance [4,5]. The spatiotemporal patterns of evapotranspiration (ET) have long been a focal point of scientific investigation, with extensive research conducted at both global and regional scales. Accurately quantifying the process of ET and examining its response to climate change and shifts in vegetation cover is not only of profound significance in scientific research but also indispensable in addressing real-world challenges. In essence, understanding the dynamics of ET is crucial for predicting the impacts of environmental alterations and formulating adaptive strategies [5–7]. The study aims to deepen our understanding of the water cycle within ecosystems and shed light on how these complex processes are affected by changes in external environmental conditions. This approach provides a solid basis for the formulation of locally appropriate policies for water resources management and ecosystem protection [8–10].

In traditional evapotranspiration calculations, point-scale measurements are usually used. This approach has limitations when obtaining large-scale regional data [11]. As remote sensing technology has advanced, it has proven to be a valuable tool for tracking and assessing extended trends in evapotranspiration over expansive regions. This progress is due to its extensive monitoring capabilities, regular monitoring functions, and the collection of real-time data [3,12–15]. In arid or semi-arid regions, investigating the quantitative relationship between evapotranspiration (ET) and its drivers is crucial. Researchers like Jin et al. [16] have employed ET models to isolate the effects of vegetation restoration and climate change on ET by controlling variables, finding that vegetation recovery is the critical factor increasing ET. In their study, Fu and colleagues examined the typical effects of rainfall, potential evapotranspiration, and reforestation efforts on alterations in evapotranspiration rates. Their findings suggest that precipitation plays a pivotal role in shaping these fluctuations in evapotranspiration. These studies have effectively separated the effects of climate change and vegetation shifts on evapotranspiration through their models and simulations. However, the parameters of these models can be impacted by various factors such as plant type, climatic conditions, and soil properties, which introduces some uncertainty when identifying the causes behind evapotranspiration variations [17–21]. Wang et al., through stepwise regression analysis, identified vegetation change as the primary cause of increased ET [22]. In comparison, regression analysis, as a more straightforward statistical approach, is often used for quantifying analysis of the driving factors of evapotranspiration [23]. However, this method is not sufficient to quantify the specific contributions of individual influencing factors, thus presenting certain limitations when it comes to objectively evaluating the eco-hydrological effects in the particular region of the JRB. This indicates that, while regression analysis is straightforward to operate, more refined research and technical support are needed to deeply explore the complex mechanisms behind evapotranspiration and the actual impacts of various factors.

The PT-JPL model, due to its incorporation of dynamic vegetation information and an evapotranspiration mechanism, facilitates a more accurate simulation of the evapotranspiration process across different environment conditions, elucidating the interaction among elements of hydrological cycle under complex hydrothermal scenarios [24]. When simulating evapotranspiration, especially at the interannual scale, the PT-JPL model yields simulation closely aligned with observed values. At the regional scale, the model can integrate remote sensing data and meteorological data to simulate a large-scale evapotranspiration process [25].

The Jing River, a critical component of the Yellow River system, is inextricably linked to the Northwest Loess Plateau region. It is not only an area that responds swiftly to climate fluctuations but also a fragile zone susceptible to ecological imbalance. Moreover, it is pivotal in soil and water conservation efforts in the middle and upper reaches of the Yellow River [26,27]. Conducting a comprehensive and detailed investigation into the environmental challenges confronting the river basin and devising effective strategies to foster sustainable agricultural development and ecological restoration are of paramount importance, both academically and practically. Such efforts will aid in the protection and enhancement of the local ecological environment while transforming and upgrading local agricultural production models to accommodate evolving natural conditions and socio-economic demands. In large-scale vegetation restoration and construction projects, the inappropriate selection of tree species for restoration could lead to new ecological problems.

To advance the scientific understanding of water resources management and utilization strategies in the Jing River Basin, this study aims to enhance the timeliness and reliability of the previous research findings over 40 years [26]. The current study focused on the period from 1984 to 2018, providing a detailed quantitative analysis of evapotranspiration dynamics in the Jing River Basin. Given the potential limitations of historical data for existing decision support systems, advanced time series analysis and high-precision meteorological and hydrological data are utilized to uncover the principal drivers of evapotranspiration in the Jing River Basin. This endeavor is intended to furnish local governments with more accurate, timely advice on water resources management. It not only fills a gap in existing research for specific periods, but also by identifying environmental and human factors that dominate evapotranspiration changes, it provides a solid scientific basis for the sustainable utilization of water resources and the policy-making of ecological protection in the basin. At the same time, due to the complex relationship among climate, vegetation, and hydrological cycles, the influence of recent meteorological factors on JRB evapotranspiration and their direct contribution have not been fully included in previous studies. The key factors influencing evapotranspiration in the Jing River Basin in recent years remain unclear. This necessitates additional, comprehensive research to identify these critical elements, thereby enhancing our ability to accurately comprehend and forecast hydrological dynamics and ecosystem responses within the basin.

Given this, the project employed the PT-JPL model to simulate evapotranspiration within the Jing River Basin. It quantitatively assessed the driving mechanisms of climate change and vegetation change on evapotranspiration spatiotemporal evolution. According to the research objectives of this paper, we make the following assumptions: (1) regional vegetation greening will increase evapotranspiration; (2) climate change and vegetation greening will have a synergistic effect on the increase in regional evapotranspiration; (3) climate change and vegetation greening not only drive the evapotranspiration process directly but also change the evapotranspiration process indirectly through their interaction. The results of this study have significant reference value for regional water resources management and sustainable vegetation restoration strategy.

2. Material and Methods

2.1. Study Area

The Jing River watershed occupies a central position within the Loess Plateau region (between longitude 106°20'~108°20' E and latitude 34°24'~37°48' N), originating from the

Liupan Mountain and flowing through the Northwest Loess Plateau [28]. The Jing River traverses the regions of Ningxia, Gansu, and Shaanxi before joining the Wei River within the jurisdiction of Gaoling County. The area encompasses approximately 45,400 square kilometers and comprises seven urban centers and twenty-seven county regions spanning three different provinces, characterizing it as a representative basin within the vegetation rehabilitation zone of the Loess Plateau [18,29]. The underlying geologic framework plays a significant role in shaping the intricate landforms found within the area. The geologic framework of this area contributes to its intricate landscape. The composition of the earth here closely resembles that found on the eastern side of Gansu's Loess Plateau, characterized by extensive layers of Quaternary sediments at the surface. The basin is situated in the Wei he Rift Valley, with most of its expanse occupying the east of Gansu's Loess Plateau. This location presents a significant altitude variation, ranging from 359 m to 2896 m above sea level [30] (Figure 1a). In the Jing River Basin, both precipitation and temperature gradually rise as one moves southward. In the summer, the mercury can be as high as 15 degrees Celsius. At the same time, in the winter, the thermometer can be as low as 1 degree Celsius (Figure 1b). Annual precipitation varies significantly, ranging from 296 to 611 mm, with an average annual rainfall of 510.8 mm. (Figure 1c). The primary land cover types include forests, grasslands, farmland, shrubland, desert, and other vegetation (Figure 1d).

2.2. Data Sources and Processing

2.2.1. Remote Sensing Data

This study utilizes GLASS leaf area index (LAI) products for its analysis "<https://www.geodata.cn/> (accessed on 26 December 2022)". Multiple remote sensing indicators were utilized to drive the PT-JPL model, such as the normalized difference vegetation index (NDVI), leaf area index (LAI), and land cover type data [31]. The NDVI data applied in this research originated from the Global Inventory Modeling and Mapping Studies (GIMMS) NDVI 3g V3.1 product "<https://ecocast.arc.nasa.gov/data/pub/gimms/3g.v1/> (accessed on 8 October 2022)".

The dataset encompasses a spatial granularity of 0.05 degrees and updates at intervals of 15 days, spanning the years from 1984 to 2018. Key variables such as leaf area index (LAI) and surface albedo are predominantly derived from the Global Land Surface Satellite (GLASS) series, which offers these metrics at a spatial precision of 0.05 degrees and a temporal frequency of once every eight days. Additionally, land cover information, presented at a spatial scale of one kilometer, is retrieved from the National Earth System Science Data Center [32,33] "<https://www.geodata.cn/> (accessed on 5 June 2022)". This source supplies land cover mapping products that are updated every seven years (1980, 1990, 1995, 2000, 2005, 2010, and 2015). In this study, our analysis period is set from 1984 to 2018 [17]. To streamline the data preparation process, we assume that the land cover status remained unchanged between 1980 and 1984, and we use the 1980 land cover data as a baseline for the classification in 1982. We reclassified the original land cover data into five main categories: forest, grassland, cropland, shrub, and barren land. To ensure the accuracy of the analysis, we excluded areas where land cover types changed during the study period, focusing only on regions with stable land cover types. Using the bilinear interpolation technique in the ArcGIS 10.8 software (Environmental Systems Research Institute, Redlands, CA, USA), we resampled all datasets to a uniform 1 km spatial resolution to facilitate effective integration and subsequent analytical work.

2.2.2. Meteorological Data

To ensure the accuracy of the meteorological data, we utilized a reanalysis dataset containing near-surface meteorological and environmental parameters, carefully assembled by experts at the Institute of Tibetan Plateau Research under the auspices of the Chinese Academy of Sciences "<http://data.tpdc.ac.cn> (accessed on 20 November 2022)". Our climate factor data combine various global datasets such as Princeton reanalysis data,

GLDAS information, GEWEX-SRB radiation data, and TRMM precipitation records, along with traditional meteorological observations from the China Meteorological Administration. Spanning the years 1979 to 2018, it offers a three-hourly temporal resolution and a 0.1-degree spatial resolution, encompassing seven key elements: 2 m air temperature, air pressure, specific humidity, 10 m wind speed, downward shortwave and longwave radiation, and surface precipitation rate.

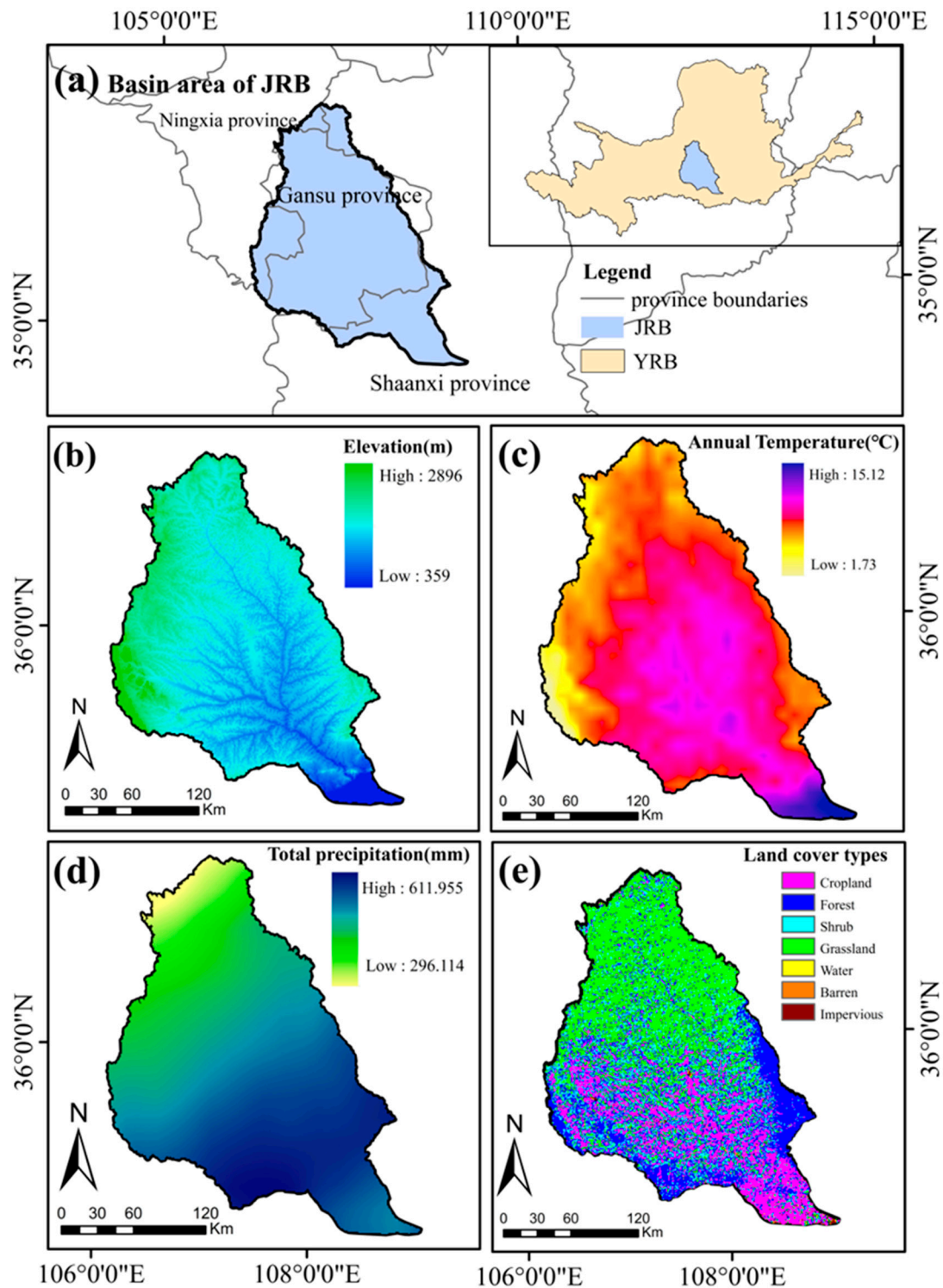


Figure 1. (a) Study area; (b) elevation; (c) annual temperature; (d) total precipitation; and (e) land cover type in the JRB.

In the conducted research, the methodology employed involves deriving the magnitude of wind velocity at a height of approximately two meters above the ground level (WS), utilizing a specified mathematical formula referred to as Equation (1) as the computational framework [34]:

$$wind_2 = wind_{10} \frac{4.87}{\ln(67.82 - 5.42)} \quad (1)$$

In this case, $z = 10$ m, $wind_2$ represents the near-surface 2 m, and 2 metering and $Wind_{10}$ represent the near-surface 10 m and 10 metering [35,36].

Estimate VPD based on Equations (2) and (3):

$$RH = 0.263pq \left[e^{\left(\frac{17.67(T-T_0)}{T-29.68} \right)} \right]^{-1} \quad (2)$$

$$VPD = 0.61078 \times e^{\frac{17.27 \times (T-273.16)}{T-273.16+237.3}} \times (1 - RH) \quad (3)$$

where p is the atmospheric pressure (Pa); T is the temp (K); T_0 is the reference temp (273.16 K usually). q is specific humidity (dimensionless). RH is relative humidity.

Calculated Rad was according to Equation (4):

$$Rad = LRad + SRad \quad (4)$$

where $LRad$ represents downward longwave radiation, Rad stands for the total radiation, and $SRad$ denotes downward shortwave radiation.

2.3. Methods

2.3.1. Priestley–Taylor Jet Propulsion Laboratory Model

By introducing a series of parameters to constrain the coefficients in the model, the model can be parameterized and applied to different ecosystems and climate conditions. In parameterization, we use a sensitivity analysis method to identify the parameters in the model that have the most influence on the simulation results. This method can help researchers find the best combination of parameters to improve the simulation accuracy and reliability of the model. In addition, this study also deals with the constraints of bio-meteorological methods on the coefficient, as well as the consideration of factors such as relative humidity, soil moisture, and canopy coefficient, so that the model can more accurately calculate the interception evaporation, soil surface evaporation, vegetation transpiration, and water surface evaporation components of evapotranspiration. Finally, the parameterization of the PT-JPL model needs to be adjusted and calibrated according to the ecosystem characteristics and available data of a specific study area [25].

The PT-JPL model, through its quantification of these three evapotranspiration components, provides a more precise description of the surface hydrological cycle, aiding in a deeper understanding of water dynamics and energy balance within ecosystems. The utilization of this technology extends across a diverse array of domains, including studies on environmental shifts, the oversight of aquatic resources, and evaluations of ecological systems' well-being [37,38]. The specific formula is as follows:

$$ET = E_c + E_s + E_i \quad (5)$$

$$T = (1 - f_{wet}) f_g f_t f_m \alpha \frac{\Delta}{\Delta + \gamma} R_{nc} \quad (6)$$

$$ES = (f_{wet} + f_{sm}(1 - f_{wet})) \alpha \frac{\Delta}{\Delta + \gamma} (R_{ns} - G) \quad (7)$$

$$LE = f_{wet} \alpha \frac{\Delta}{\Delta + \gamma} R_{nc} \quad (8)$$

In the given equation, α takes a value of 1.26 (dimensionless), which represents the adjustment coefficient of the Priestley–Taylor model. It usually takes a value between 1.25 and 1.31, whereas in the PT-JPL model, it usually takes 1.26; this factor is used to adjust the potential evapotranspiration calculated by the model to be closer to the actual evapotranspiration, while γ denotes the second coefficient, referred to as the dry-to-wet constant, having a value of 0.066 kPa/°C. The symbol Δ signifies the gradient of the curve representing saturated vapor pressure (kPa/°C). Furthermore, R_{ns} stands for the net radiation absorbed by the soil ($\text{W}\cdot\text{m}^{-2}$), which can be computed utilizing the formula: $R_{ns} = R_{nc}^{-kR_nLAI}$, wherein kR_n signifies the extinction coefficient, set at 0.6 (dimensionless). Additionally, R_{nc} refers to the net radiation incident upon the canopy ($\text{W}\cdot\text{m}^{-2}$), which can be represented as $R_{nc} = R_n - R_{ns}$ [17]. The computations and explanations related to the bio-physiological constraint factors, namely, (f_{wet} , f_g , f_t , f_m and f_{sm}), along with the determination of the soil heat flux (G) ($\text{W}\cdot\text{m}^{-2}$).

The calculation describing the relative humidity (f_{wet}) is shown in Equation (9):

$$f_{wet} = RH^4 \quad (9)$$

Use Equations (10)–(12) to calculate the green canopy fraction (f_g):

$$f_g = \frac{f_{APAR}}{f_{IPAR}} \quad (10)$$

$$f_{APAR} = b_1 \times \left(1 - e^{-k_1 \times LAI}\right) \quad (11)$$

$$f_{IPAR} = b_2 \times \left(1 - e^{-k_2 \times LAI}\right) \quad (12)$$

In the formula given, f_{APAR} and f_{IPAR} represent the proportion of photosynthetic effective radiation absorbed and intercepted by vegetation canopy, respectively. Constants b_1 and b_2 , which are set to 0.95 and 0.9355, respectively, are critical for calculating f_{APAR} and f_{IPAR} [39,40].

Plant temperature constraints (f_t) are calculated using Equation (13):

$$f_t = \exp\left(1 - \left(\frac{T_{max} - T_{opt}}{T_{opt}}\right)^2\right) \quad (13)$$

In addition to the optimum temperature for plant growth (T_{max}) and the optimum temperature for plant growth (T_{opt}), environmental factors are added, and examples are relative humidity (RH^4) and vapor pressure deficit (VPD).

Use Equation (14) to calculate plant moisture constraint (f_m):

$$f_m = \frac{f_{APAR}}{f_{APAR_{max}}} \quad (14)$$

Fraction of PAR (f_{sm}) are calculated using Equation (15):

$$f_{sm} = RH^{VPD/\beta} \quad (15)$$

Ground heat flux (G) is calculated using Equation (16):

$$G = R_n \left[\Gamma_c + \left(1 - \frac{NDVI - NDVI_{min}}{NDVI_{max} - NDVI_{min}}\right) (\Gamma_s - \Gamma_c) \right] \quad (16)$$

The model includes a parameter β , which indicates the response of soil moisture limitation to VPD in a range between 0 and 1. The net radiation (R_n) is quantified in ($\text{W}\cdot\text{m}^{-2}$). Furthermore, Γ_c was equal to 0.05, a parameter characterizing regions with increased vegetation coverage, whereas Γ_s was set to 0.325, indicating regions with improved bare

soil conditions [17,38]. The sensitivity of the PT-JPL model is significantly affected by its key parameters k_1 , k_2 , and β , which have been fine-tuned for a variety of ecosystems to improve model accuracy [17]. In this study, the model parameters were adjusted according to the optimization of different vegetation types by our research group [17].

The specific parameters were adjusted as follows: forest, $k_1 = 0.57$, $k_2 = 0.81$, $\beta = 1.28$; grassland, $k_1 = 0.59$, $k_2 = 0.80$, $\beta = 0.80$; cropland, $k_1 = 0.59$, $k_2 = 0.84$, $\beta = 1.43$; shrubland, $k_1 = 0.56$, $k_2 = 0.91$, $\beta = 1.17$.

2.3.2. Trend Analysis

The Theil–Sen estimator is used to estimate time trends in time series data as a nonparametric method. Due to its insensitivity to abnormal observation results and measurement errors, this method is suitable for trend analysis in a wide range of time series datasets. The estimation of the Theil–Sen parameter is facilitated by utilizing its prescribed Equation (17):

$$\text{Slope} = \text{Median}\left(\frac{X_j - X_i}{j - i}\right), \forall i < j \quad (17)$$

In the formula, the slope represents the median estimated slope when $i \neq j$; X_j and X_i represent the values of variable X in the i -th and j -th years, and i and j are used to represent years. When a variable shows an increasing trend within a given time series, it is represented by a $\text{Slope} > 0$. Conversely, the $\text{Slope} < 0$.

2.3.3. Mann–Kendall Test

The Mann–Kendall method analyzes the general trend in time-series data, which can show no trend, an increase, or a decrease. When no trend is detected, the data points are considered independent and identical across time, with no ongoing connection to them. The Mann–Kendall test does not demand a normal distribution of the data or a linear nature of the trend change. Even with missing values or data below certain thresholds, the test can still be performed, albeit potentially with reduced effectiveness. For the test's validity, it assumes that the intervals between samples are sufficiently long to ensure that measurements taken at different times are uncorrelated.

The data are taken out in sequence according to the collection time, where $X = (X_1, X_2 \dots X_n)$, and where n is the number of samples. Use Equations (18) and (19) to test the calculation formula for the statistic S .

$$S = \sum_{i=1}^{n-1} \sum_{j=i+1}^n \text{sgn}(X_j - X_i) \quad (18)$$

$$\text{Sgn}(X_j - X_i) = \begin{cases} +1, & X_j - X_i > 0 \\ 0, & X_j - X_i = 0 \\ -1, & X_j - X_i < 0 \end{cases} \quad (19)$$

When S represents a value greater than zero, the data points towards the end of the observation period are likely to exhibit a higher trend than those recorded earlier. Conversely, if S assumes a value less than zero, the latter observed data points are expected to show a decline relative to their preceding counterparts.

Calculate the variance $\text{Var}(S)$ using Equation (20):

$$\text{Var}(S) = \frac{n(n-1)(2n+5) - \sum_{i=1}^n t_i(i-1)(2i+5)}{18} \quad (20)$$

where t_i represents the number of members in the i group with equal data sets. Calculate the standardized statistic Z using Equation (21)

$$Z = \begin{cases} \frac{S-1}{\sqrt{\text{Var}(S)}}, S > 0 \\ 0, S = 0 \\ \frac{S+1}{\sqrt{\text{Var}(S)}}, S < 0 \end{cases} \quad (21)$$

At a given significance level α , the rejection of the null hypothesis (H_0) suggests that there is a statistically significant trend with a confidence level of $1 - \alpha$. Conversely, accepting the null hypothesis implies that the observed trend lacks statistical significance. A positive Z value signifies an increasing trend within the dataset, whereas a negative Z value points towards a decreasing trend.

2.3.4. Partial Correlation

Partial correlation (PC) serves as a technique to assess the strength of association between two variables while controlling for the influence of a designated variable. In a scenario where a correlation analysis involving three variables reveals a correlation among all three, it is necessary to isolate the effect of the third variable prior to examining the correlation between the first and second variables. When considering the influence of a single control variable, the resulting measure is referred to as a first-order partial correlation coefficient. Conversely, when accounting for the effects of two control variables, the measure employed is known as a second-order correlation coefficient. This approach takes into account the complex interplay among various variables in determining their relationships. Calculate the partial correlation coefficient of x_1 and y_1 using Equation (22):

$$r_{y1,2} = \frac{r_{y1} - r_{y2}r_{12}}{\sqrt{(1 - r_{y2}^2)(1 - r_{12}^2)}} \quad (22)$$

In this formula, r_{y1} , r_{y2} , and r_{12} represent the correlation coefficients between y and x_1 , y and x_2 , and x_1 and x_2 . The absolute value of the partial correlation coefficient (PCC) can indicate the degree of direct correlation between two variables. A larger absolute value indicates a stronger linear correlation, while a weaker correlation indicates a smaller value. In this study, the partial correlation coefficients of six driving factors concerning ET were calculated.

2.3.5. Attribution Analysis

Normalize all raw data using Equation (23):

$$X_i = \frac{x_i - x_{min}}{x_{max} - x_{min}} \quad (23)$$

where X_i is normalized data; x_{max} and x_{min} represent the maximum and minimum values of the sample data; and x_i refers to the annual data of the sample.

Multiple regression analysis (MRA) is used to calculate the contribution of various driving factors in JRB to ET. Calculate using Equations (24) and (25):

$$Y_{ET} = b_0 + b_1X_1 + b_2X_2 + \dots + b_iX_i + \mu \quad (24)$$

$$W_{ba_i} = \frac{b_iX_{i,rend}}{Y_{ET_{a_i,rend}}} Y_{ET_{n_i,rend}} \quad (25)$$

Among them, Y_{ET} represents normalized ET; b_0 represents constant error, respectively, μ indicates system error; and b_i indicates the standard regression coefficient. The contribution of each driving factor to the trend of ET is represented by W_{ba_i} ; $Y_{ET_{n_i,rend}}$ refers to the actual trend of ET; the trend of normalized ET is shown in $Y_{ET_{a_i,rend}}$.

To identify the primary influences on evapotranspiration (ET) variations through a systematic approach, we aim to pinpoint the regulatory element exerting the least detri-

mental effect on regions experiencing a decline in *ET*. Additionally, we assess the proportional impacts of precipitation, air temperature, radiation, wind speed, vapor pressure deficit, and leaf area index on fluctuations in *ET* levels.

2.3.6. Pathway Analysis Method

Path coefficient analysis is a statistical methodology that can investigate the direct relationships among multiple predictor variables and one outcome variable through linear connections. It builds upon regression analysis and can handle intricate relationships among variables where numerous independents are interconnected or where specific independents influence the dependent variable indirectly through other factors. The structural equation model, composed of a group of linear equations, reflects the relationships among independent variables, mediating variables, latent variables, and the dependent variable, and it quantifies the impact of these variables on each other accurately. Path coefficients serve as dimensionless comparative figures, quantifying the magnitude of the direct influence that independent variables exert on a dependent variable. These values facilitate the assessment of the relative significance of each predictor variable. Path analysis can establish an “optimal” multiple regression equation, thereby better understanding the relationships among variables [41–43].

2.4. Technology Road

Figure 2 clearly shows the research process of this study. In order to study the synergistic effects of climate and vegetation on evapotranspiration in Jing River Basin, leaf index, net radiation data set, evapotranspiration data set and land use data set were obtained, and Arcgis 10.8 software (Environmental Systems Research Institute, Redlands, CA, USA), was used for data processing. By using the PT-JPL model optimized by MATLAB 2023a software (Shanghai Pudong New Area MathWorks Company, Shanghai, China), we analyzed the data and obtained the spatiotemporal evolution characteristics and change rules of meteorological elements and vegetation evapotranspiration at the annual scale. Origin software (OriginLab Company, Northampton, MA, USA) was used for mapping to reveal the correlation between meteorological elements and evapotranspiration and the spatiotemporal changes of evapotranspiration in different vegetation types. It provides theoretical basis for the practice of sustainable water resources management in Jing River Basin.

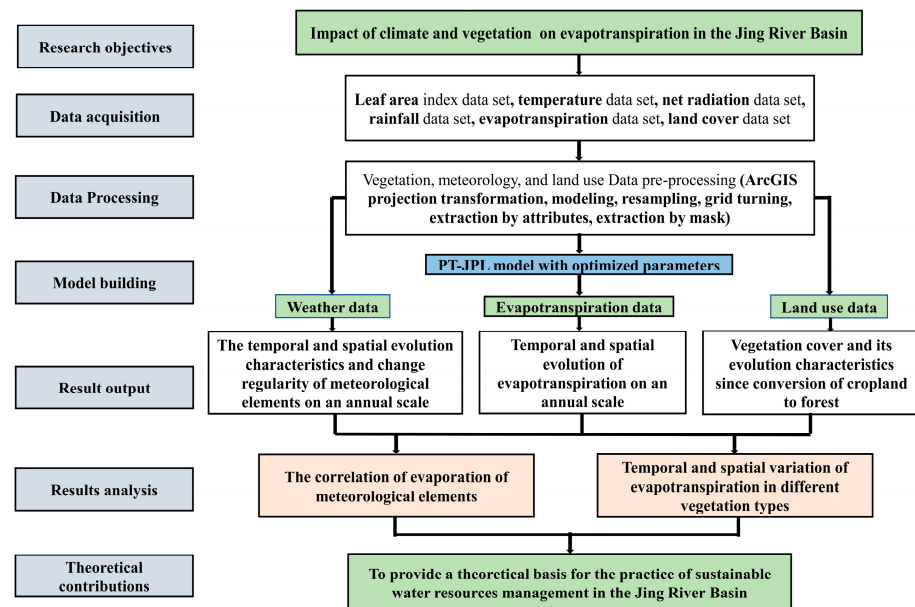


Figure 2. Technology roadmap.

3. Results

3.1. Validation of Evapotranspiration Simulation Based on Water Balance

To validate the accuracy of ET simulation using the PT-JPL model, we calculated ET for the watershed based on the water balance method. Specifically, we obtained annual runoff data for the watershed from the Gansu Provincial Water Conservancy and Hydroelectric Power Bureau. We used the water balance formula $ET = P - Q - \Delta S$ to calculate the water balance ET, where P, Q, and ΔS represent the precipitation, runoff, and changes in soil moisture within the watershed, respectively. It should be noted that the runoff data are based on the monitoring of the Zhangjiashan hydrological station in the Jing River Basin. The multiyear averaged water storage is assumed to be constant [16]. Meanwhile, Shao and his colleagues also point out that changes in soil water over many years in Some Random Place Somewhere areas are negligible [44]. Consequently, the multiyear averaged water storage ET is calculated as the annual P minus the annual Q. As shown in Figure 3, the annual precipitation and annual runoff in the Jing River Basin show an upward trend. In contrast, the water balance ET shows an upward trend; this is consistent with our simulated ET trends. To further verify the accuracy of our simulation, we used the determination coefficient and root mean square error and used regression analysis to reveal the correlation between water balance ET and simulated ET. The results show that there is a high correlation between PT-JPL ET and water balance ET with a determination coefficient of 0.98 and a root-mean-square error of 11.016, which confirms that our simulation results are reliable in the Jing River Basin and can be used for subsequent analysis.

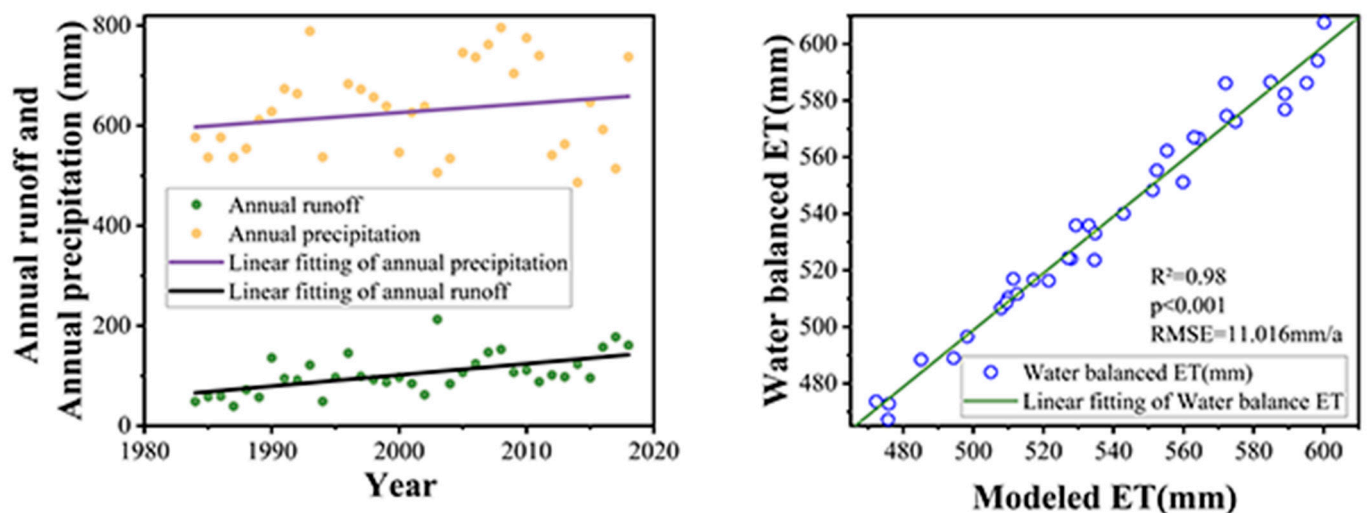


Figure 3. The annual precipitation, yearly runoff, and examination of the variance between the three-year mean estimated evapotranspiration (ET) and the ET derived from the water balance approach across twelve distinct sub-catchments within the Jing River Basin over the period spanning from 1984 to 2018.

3.2. Spatiotemporal Variations of ET

3.2.1. Annual Interannual Trends in Evapotranspiration

As shown in Figure 4, the annual evapotranspiration (ET) in the Jing River Basin ranges from 472 to 600 mm, with an average value of 538 mm. Overall, from 1984 to 2018, ET showed a significant increasing trend with fluctuations ($p < 0.01$), with an interannual rate of change of 3.05 mm/year. There was little change from 1984 to 1995, after which it began to fluctuate significantly. In 1989, the ET value was the smallest, 66 mm lower than the average. By land type, the order of ET is Forest > Cropland > Shrub > Grassland.

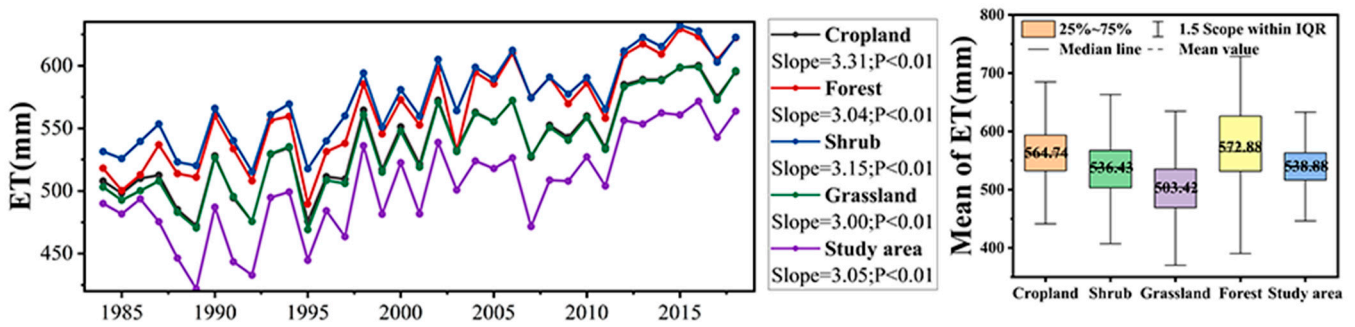


Figure 4. Annual interannual trends in evapotranspiration.

3.2.2. Spatial Distribution, Temporal Trends, and Significance of ET Changes

In the illustration shown in Figure 5, a clear trend can be observed that the annual mean evapotranspiration rate shows a continuous decreasing trend as it moves from the southeast coastal area to the northwest inland area. The spatial distribution of evapotranspiration in Jing River Basin reflects the spatial distribution of annual precipitation in China, with higher evapotranspiration mainly occurring in the southwest and southern parts of the basin. On the contrary, the northern Jing River Basin showed a lower ET value (Figure 5a). The temporal trend and significance of ET change during 1984–2018 were analyzed, and the results showed that ET showed an increasing trend in most areas of the study area. The change of ET in the eastern region is stronger than that in the western region. Some central parts of the study area showed no discernible ET changes (Figure 5b). Geographically, the significant increase in ET was concentrated in the western part of the basin (Figure 5c). Among them, the ET in the southeast of the basin decreased most obviously, and the change rate was -0.19 mm/year. Land types according to the rate of change in the comparison, the cultivated land (3.33) > shrub (3.17) (3.02) > grassland > forest (2.90).

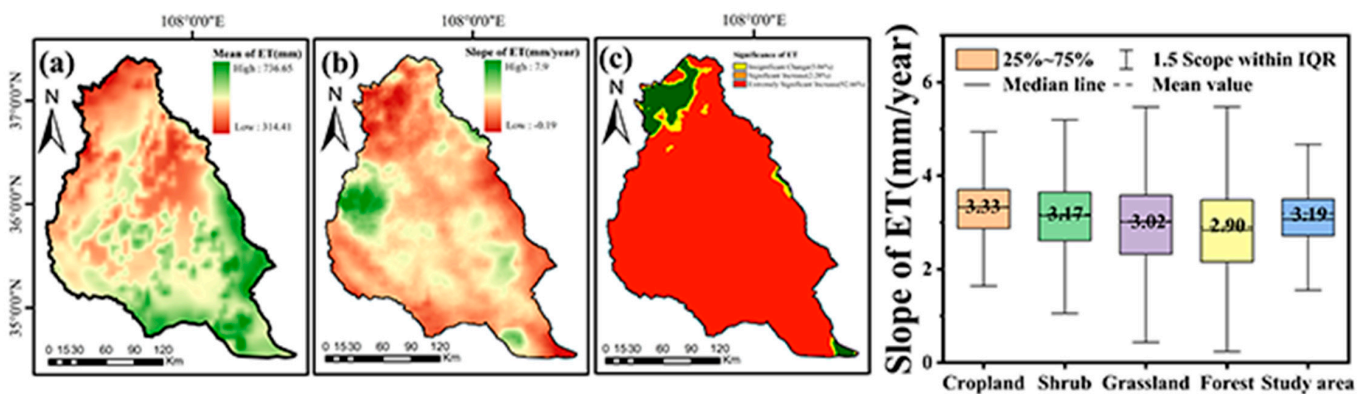


Figure 5. Investigate the spatial dispersion traits of the yearly mean, as well as the geographical trends and statistical assessments of alterations in Evaporation (ET) and its constituent elements across the Jing River Basin (JRB) between 1984 and 2018.

3.3. Temporal–Spatial Characteristics of LAI and Climatic Factors

3.3.1. The Temporal–Spatial Characteristics of LAI and Climatic Factors

As shown in Figure 6, the leaf area index (LAI) ranged from 0.96 to 2.16 mm^2/mm^2 from 1984 to 2018, with an average value of 1.45 mm^2/mm^2 . Overall, from 1984 to 2018, the LAI fluctuated and increased (with a significance level of $p < 0.1$), with an interannual rate of change of 0.03 $\text{mm}^2/\text{mm}^2/\text{year}$. The largest LAI since 1984 occurred in 2018, exceeding the average by 0.71 mm^2/mm^2 . The smallest LAI was recorded in 1997, which was 0.49 mm^2/mm^2 below the average (Figure 6a). The annual radiation values varied between 451 and 477 W/m^2 , with an average of 467 W/m^2 and overall large fluctuations and an upward trend, with an interannual rate of change of 0.41 $\text{W}/\text{m}^2/\text{year}$ (Figure 6b).

Precipitation showed overall large fluctuations and an increasing trend, ranging from 338 to 745 mm, with an average of 512 mm and an interannual rate of change of 1.9375 mm per year; however, its correlation with ET was not significant (Figure 6c). Temperature exhibited an overall upward trend, with a downward trend from 1998 to 2010, at an interannual rate of change of 0.07 °C per year, with the lowest temperature occurring in 1984 and the highest in 2017 (Figure 6d). Wind speed showed an overall upward trend, with a decline from 2000 to 2010 and large fluctuations, at an interannual rate of change of 0.01 m/s/year (Figure 6e). The saturated vapor pressure displayed large fluctuations and an overall increasing trend, with an interannual rate of change of 0.004 kPa per year (Figure 6f).

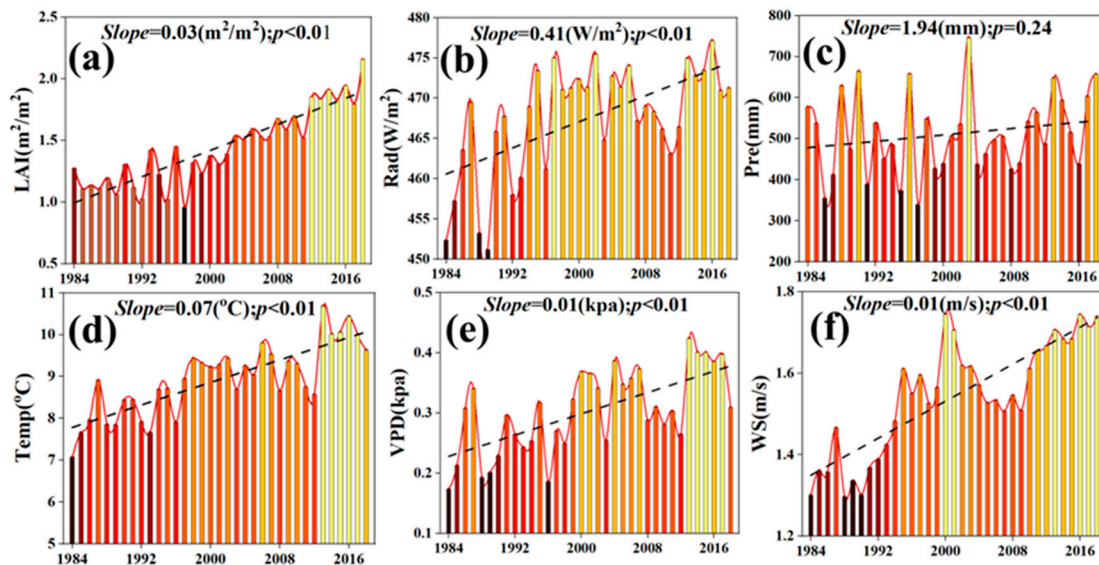


Figure 6. The temporal–spatial characteristics of LAI and climatic factors (Rad (Radiation), Pre (Precipitation), Temp (Temperature), VPD (Vapor pressure difference), WS (Weed speed)).

3.3.2. Multiyear Mean Spatial Distribution Patterns of LAI and Climatic Factors

As depicted in Figure 7, the leaf area index (LAI) has experienced more growth in the western and eastern marginal areas of the JRB, with smaller increases in the middle region transitioning gradually towards the margins, where the LAI values are higher, including areas west and south of Xifeng City, and lower values in areas such as Baoji City, southern Yan'an, and Northwest Xi'an (Figure 7A-1). Among different vegetation types, forests have the highest average annual LAI ($2.12 \text{ mm}^2/\text{mm}^2$), followed by croplands ($1.53 \text{ mm}^2/\text{mm}^2$), while grasslands have the lowest ($0.98 \text{ mm}^2/\text{mm}^2$). In terms of radiation, the western part of the basin has seen smaller increments compared to the central area, and the margins have also shown less increase, with low radiation values in areas like Guyuan County and Xianyang City (Figure 7B-1). Overall, croplands have the highest average annual Rad ($464.84 \text{ W}/\text{m}^2$), followed by shrublands ($468.14 \text{ W}/\text{m}^2$), and forests have the lowest Rad values ($464.85 \text{ W}/\text{m}^2$) (Figure 7B-2). Precipitation decreases gradually from the southeastern part of the basin to the northwestern areas, with significant reductions in the latter (Figure 7C-1). Generally, the average annual Pre values are highest in croplands (547.52 mm), followed by forests (543.74 mm), shrublands (515.52 mm), and grasslands (1468.33 mm) (Figure 7C-2). High-temperature zones include Xi'an, Xifeng City, while low-temperature zones include Guyuan County, with high-temperature zones in Xifeng City, Pingliang City, Xianyang City, and Baoji City, and low-temperature zones in Wuzhong City and Yulin City (Figure 7D-1). There are noticeable differences in the average annual Temp among different vegetation types, with the highest TF values recorded in croplands ($9.80 \text{ }^\circ\text{C}$) and the lowest in grasslands ($8.52 \text{ }^\circ\text{C}$) (Figure 7D-2). Saturated vapor pressure has increased significantly in the northern, central, and southeastern corners of the basin, such as in Wuzhong City and Xifeng City, while other surrounding areas have shown

minimal growth (Figure 7E-1). Overall, grasslands have the highest average annual VPD (0.32 kPa), followed by shrublands (0.30 kPa), and forests have the lowest VPD values (0.28 kPa) (Figure 7E-2). Wind speeds have notably increased in the northwestern fringe regions of the basin, such as in Wuzhong City and Yulin City, with more modest rises seen in the eastern, western, and southeastern areas, including Pingliang City and Xianyang City, displaying a declining trend from northwest to southeast (Figure 7F-1). The average annual WS values for different vegetation types are highest in grasslands (1.56 m/s), followed by shrub (1.55 m/s), cropland (1.53 m/s), and forest (1.52 m/s) (Figure 7F-2).

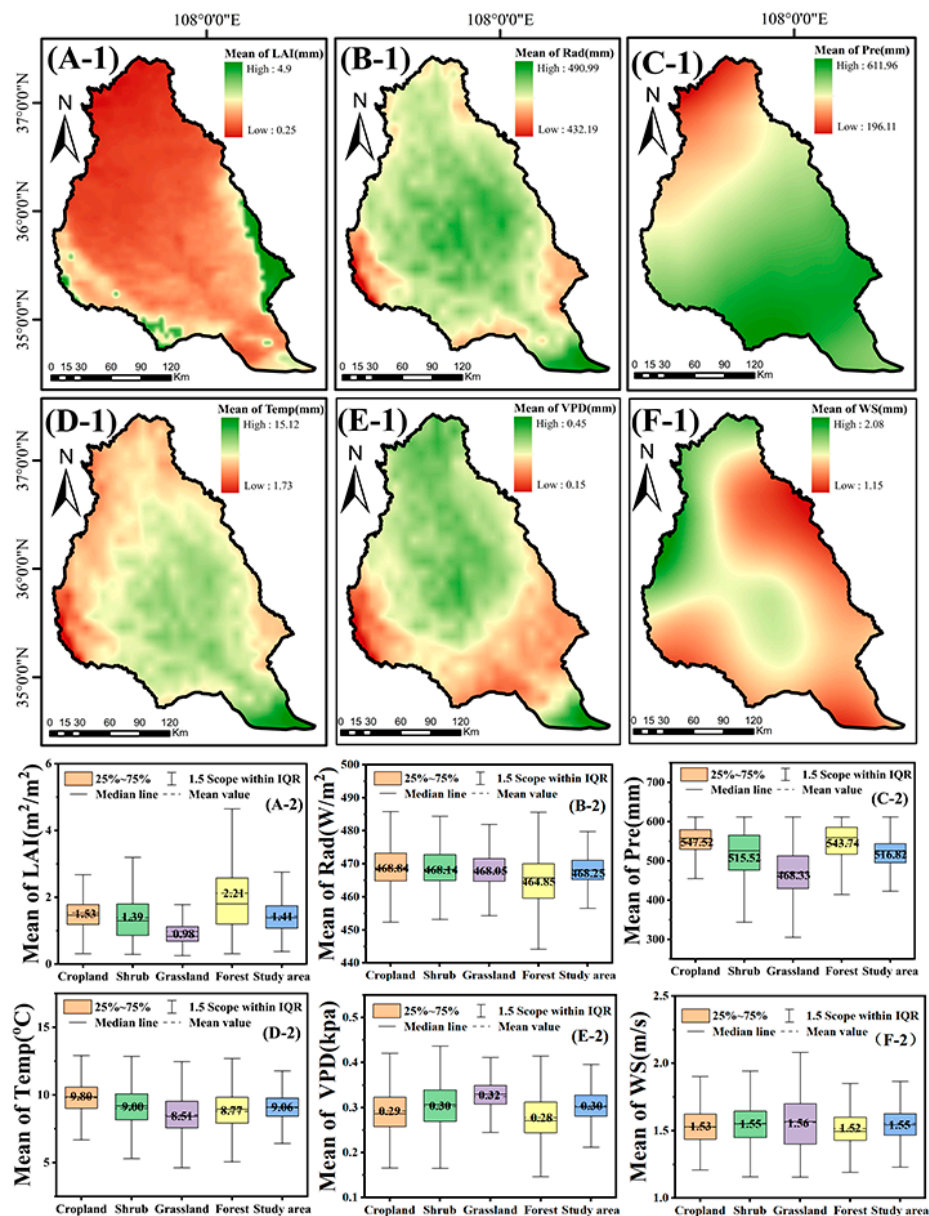


Figure 7. Spatial distributions of annual mean LAI (A-1), Rad (B-1), Pre (C-1), Temp (D-1), VPD (E-1), and WS (F-1) in the Jing River Basin from 1984 to 2018, along with the average values of different vegetation types for LAI (A-2), Rad (B-2), Pre (C-2), Temp (D-2), VPD (E-2), and WS (F-2).

3.3.3. Spatial Trends and Significance of Changes in LAI and Climatic Factors

As illustrated in Figure 8, the rate of change of the leaf area index (LAI) from 1984 to 2018 is positive, with high-value areas concentrated in the central region of the JRB, showing a significant increasing trend, while some southwest areas exhibit a substantial decrease. The pixel-based rate of change ranges from -0.024 to 0.072 mm²/mm²/year, with

an average change rate of approximately $0.0257 \text{ mm}^2/\text{mm}^2/\text{year}$ (Figure 8A-1). Among different land types, croplands have the highest increase rate ($0.032 \text{ mm}^2/\text{mm}^2/\text{year}$), followed by shrublands ($0.027 \text{ mm}^2/\text{mm}^2/\text{year}$) and grasslands ($0.025 \text{ mm}^2/\text{mm}^2/\text{year}$), with the lowest rate observed in forests ($0.021 \text{ mm}^2/\text{mm}^2/\text{year}$) (Figure 8A-2). The radiation change in the central region of the basin is small, mainly concentrated in Xifeng City, while the southern areas show significant changes, primarily in Pingliang City and Xi'an. There is a significant increase in the northern and southern parts of the basin and a notable increase in the eastern and western regions. The western parts show no change, with a pixel-based rate of change ranging from 0.16 to $0.76 \text{ W}/\text{m}^2/\text{year}$, and an average change rate of approximately $0.36 \text{ W}/\text{m}^2$ per year (Figure 8B-1). For different land types, croplands have the highest increase rate ($0.42 \text{ W}/\text{m}^2/\text{year}$), followed by forests ($0.38 \text{ W}/\text{m}^2/\text{year}$), shrublands ($0.35 \text{ W}/\text{m}^2/\text{year}$), and grasslands ($0.33 \text{ W}/\text{m}^2/\text{year}$) (Figure 8B-2). Precipitation shows no significant change within the basin. The northern and southwestern parts of the basin have reduced rainfall, while the central region has increased, especially in Xifeng City and Guyuan County, with a pixel-based rate of change ranging from 1.98 to $3.83 \text{ mm}/\text{year}$ and an average change rate of approximately $2.11 \text{ mm}/\text{year}$ (Figure 8C-1). For different land types, grasslands have the highest change rate ($2.35 \text{ mm}/\text{year}$), followed by shrublands ($2.08 \text{ mm}/\text{year}$), croplands ($1.97 \text{ mm}/\text{year}$), and forests ($1.93 \text{ mm}/\text{year}$) (Figure 8C-2). The temperature in the central region of the basin has increased significantly, including Xifeng City and Tongchuan City, with smaller increases in the southwest areas, showing a decreasing trend from the center to the edges. The basin exhibits a highly significant increase overall with a pixel-based rate of change ranging from 0.046 to $0.082 \text{ }^\circ\text{C}/\text{year}$ and an average change rate of approximately $0.0683 \text{ }^\circ\text{C}$ per year (Figure 8D-1). For different land types: grasslands have the highest change rate (0.071), followed by shrublands (0.068), croplands (0.067), and forests (0.066) (Figure 8D-2). Saturated vapor pressure has increased in the southeastern corner of the basin, including Xi'an, while it has decreased in other areas, specifically showing a gradual decrease from the edges to the central region, with a highly significant increase in the northwest and east and an average change rate of approximately $0.0044 \text{ KPa}/\text{year}$ (Figure 8E-1). For different land types, croplands have the highest change rate ($0.0051 \text{ KPa}/\text{year}$), followed by shrublands and grasslands ($0.0044 \text{ KPa}/\text{year}$), and forests ($0.0042 \text{ KPa}/\text{year}$) (Figure 8E-2). The fluctuations in wind velocity are minimal within the central area of the basin, exemplified by the city of Xifeng, whereas the southeastern edge exhibits greater variations, indicating a declining pattern moving from the southeast towards the core. The northern and western sectors, along with specific central areas of the basin, remain unchanged; conversely, discernible upward trajectories have surfaced in particular central locales, and an average change rate of approximately $0.118 \text{ m}/\text{s}/\text{year}$ was recorded (Figure 8F-1). Among the different land types, the wind speed change rate is equal for croplands and forests ($0.13 \text{ m}/\text{s}/\text{year}$), followed by grasslands ($0.12 \text{ m}/\text{s}/\text{year}$), and shrublands have the lowest rate, equal to the basin's change rate ($0.11 \text{ m}/\text{s}/\text{year}$) (Figure 8F-2).

3.4. Changes in ET Caused by Vegetation Greening and Climate Change

In order to assess the short-term impacts of diverse elements on alterations in evapotranspiration within the Jing River Basin over the period from 1984 to 2018, a technique known as partial correlation analysis was utilized to investigate the interconnections among evapotranspiration, the leaf area index, and climatic variables. The most pronounced association was found between LAI and ET, with a partial correlation coefficient (PCC) of 0.35 . Positive correlations were prevalent across the central and northwestern parts of the JRB, peaking at 0.86 , whereas negative correlations were less intense in the southeastern region, with a PCC of -0.44 (Figure 9a). The correlation coefficient between Rad and ET averages at 0.25 , exhibiting predominantly positive associations within the core zone of the JRB while manifesting negative linkages in the outer regions (Figure 9b). Examination reveals a predominantly inverse relationship between Pre and ET, characterized by a mean PCC of approximately -0.29 . Within the southwestern region, there exists a modest

positive association, peaking at 0.15. Conversely, regions beyond the southwest exhibit pronounced negative associations, attaining a level as low as -0.66 (Figure 9c). The relationship between temperature and ET exhibits the most pronounced negative association, characterized by an overall Pearson Correlation Coefficient (PCC) of approximately -0.33 . Within the core zone of the basin, this inverse connection is particularly robust, attaining a figure as low as -0.73 . Conversely, in certain southeastern pockets, there are instances of modest positive correlations, with the highest recorded being up to 0.34 (Figure 9d). The relationship between relative humidity and evapotranspiration (ET) exhibits a slight inverse association, characterized by an overall Pearson Correlation Coefficient (PCC) of approximately -0.037 . In the western regions, this connection intensifies into a robust positive correlation, peaking at a significant level of 0.47. Conversely, in the southeastern and eastern zones, the correlation shifts to a pronounced negative trend, attaining a notable magnitude of -0.48 (Figure 9e). The relationship between wind velocity and evapotranspiration (ET) exhibits a generally mild inverse association, characterized by pronounced adverse connections in the northwestern and certain southeastern regions, attaining a coefficient of -0.65 . Conversely, there are areas in the eastern part where this correlation turns positive, peaking at a value of 0.37 (Figure 9f).

The spatial distribution of contributions of leaf area index (LAI) and climatic factors to evapotranspiration (ET) changes from 1984 to 2018 is shown in Figure 9. Among these factors, the impact of vegetation greening on ET is most significant, with LAI contributing an average of 0.41 mm/year. Areas where contributions indicate an increase account for 7.9% of the total area, and the highest contribution rates are mainly located in Wuzhong City, accounting for 92.1% of the JRB (Figure 10a). The impact of Rad on ET exhibits distinct patterns across different zones. Notably, this influence predominantly diverges along the edges of the core zone within the JRB, exerting beneficial effects in the heartland while yielding detrimental consequences in the outer territories. An overwhelming majority, encompassing 97.5% of the entire expanse, demonstrates favorable contributions (Figure 10b). In terms of the impact on ET, Pre has made a negative contribution at a rate of -0.12 mm per year. Among these cities, Wuzhong primarily experiences a decrease in contributions, accounting for 97.6% of the total. In contrast, the cities of Pingliang, Xifeng, Xianyang, Tongchuan, and Xi'an predominantly exhibit an upward trend in contributions (Figure 10c). Among the climatic factors, temperature plays a pivotal role in influencing evapotranspiration (ET), with an annual increase rate of 1.5 mm. It is noteworthy that 92.44% of the studied region exhibits a decline in the temperature's contribution to ET, particularly in cities such as Xi'an, the eastern parts of Pingliang and Yan'an, as well as Xianyang and Tongchuan in the southeastern portion of the JRB (Figure 10d). In contrast, VPD contributes at a slow rate of -0.013 mm/year, gradually reducing ET. Areas with contributions less than -0.013 mm/year are concentrated in Wuzhong City, Xi'an City, Xianyang City, and Yan'an City, and these areas include certain zones with a greater decline in ET, exceeding -0.013 mm/year, accounting for 49.7% (Figure 10e). WS advances at a rate of 0.14 mm/year, with 59.6% of the total area showing growth. Regions with rates above this threshold are concentrated in the south-central part of the JRB, encompassing cities like Xifeng, Pingliang, Xianyang, Tongchuan, and Xi'an, as well as Yan'an (Figure 10f).

In Figure 11, the primary factors influencing evapotranspiration (ET) across the study area are identified. Radiation emerges as the most significant factor, contributing to 56.69% of the total ET. It is predominantly spread throughout the central region of the JRB, encompassing areas such as the center of Xifeng City, the southern parts of Guyuan, and Xianyang City. ET driven by LAI accounts for 35.61%, concentrated in the northern parts of Xifeng City and Pingliang City. Temperature tends to control ET changes in 4.68% of the study area, focused on the southern region of the JRB, such as Xi'an City and Baoji City. The remaining areas are predominantly influenced by wind speed (2.09%) and VPD (0.93%). In croplands, both temperature and radiation have the highest proportions, accounting for 41%, while in forests, radiation has the highest proportion at 54%, followed by LAI at 29%.

In shrublands, radiation has the highest proportion at 60%, and LAI accounts for 34%. In grasslands, radiation has the highest proportion at 53%, and LAI accounts for 46%.

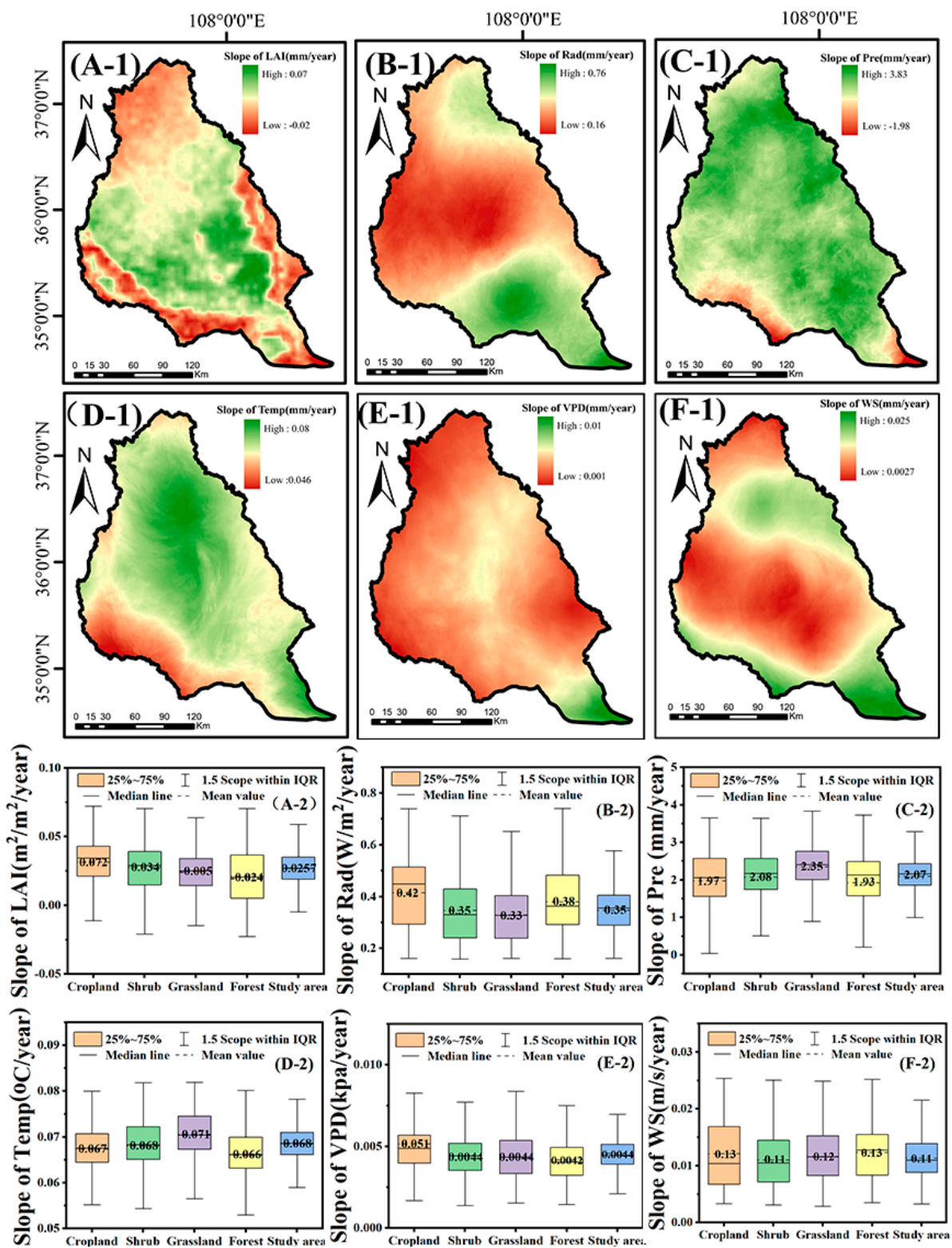


Figure 8. Spatial trends in LAI and climatic factors (Rad (Radiation), Pre (Precipitation), Temp (Temperature), VPD (Vapor pressure difference), WS (Weed speed)).

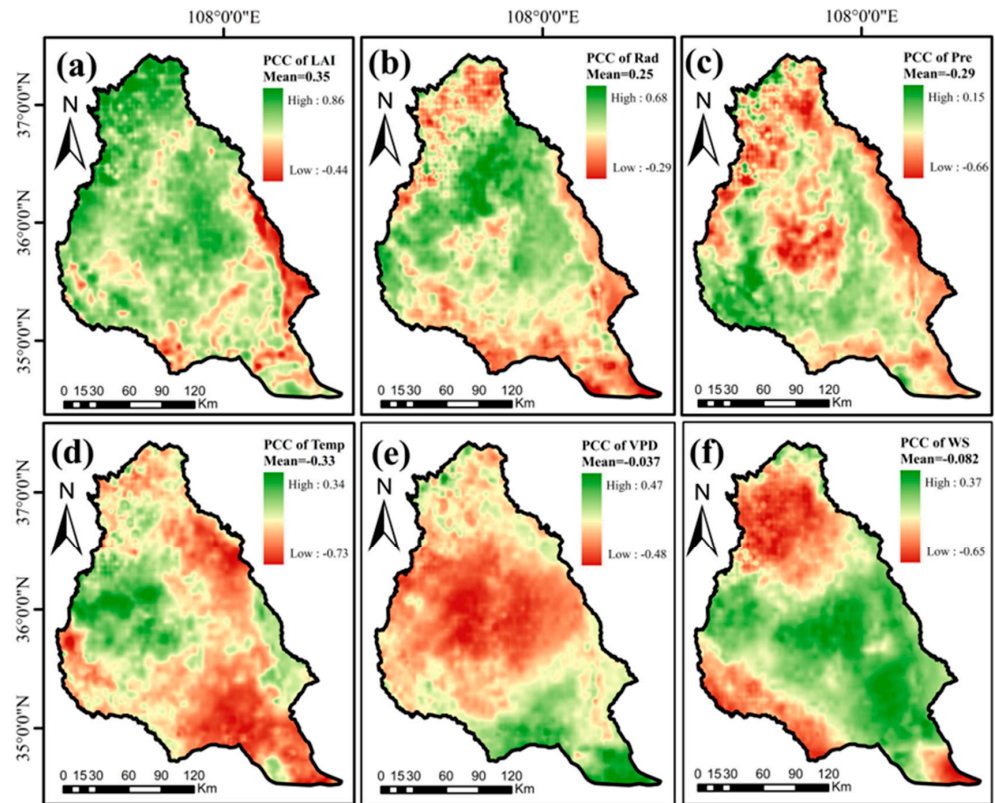


Figure 9. Investigating the regional dispersion of the associations between key determinants and evapotranspiration rates across the JRB area during the timeframe extending from 1984 through 2018, as measured by their spatial partial correlation coefficients (PCCs).

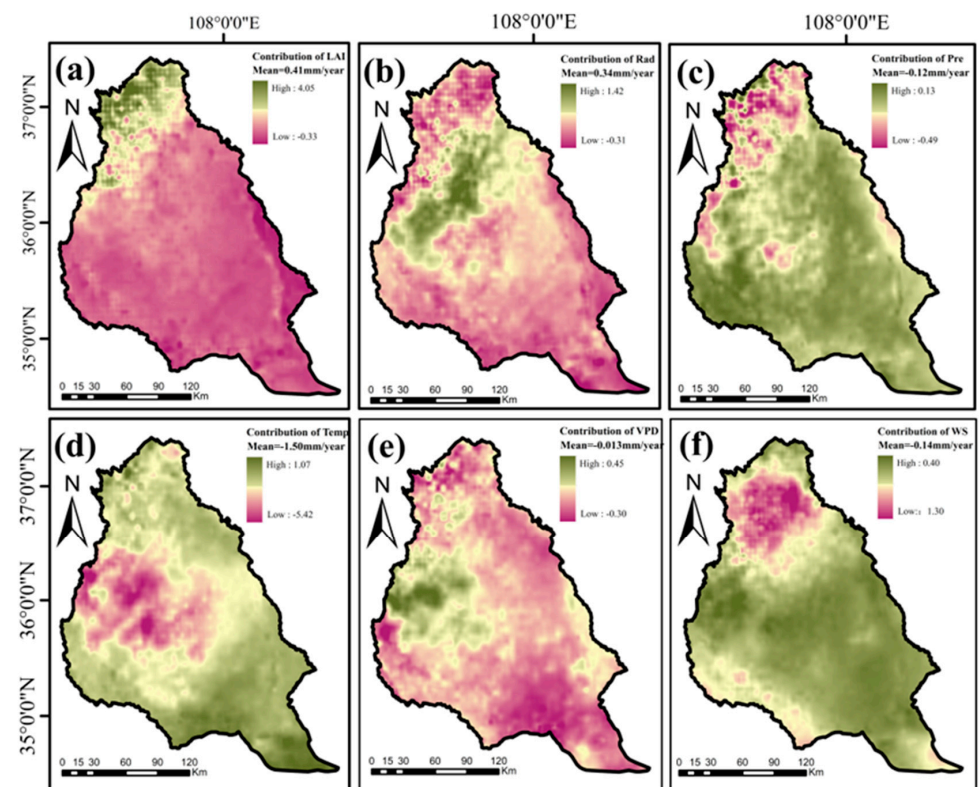


Figure 10. Spatial patterns of the absolute contributions of vegetation LAI and climate factors to the variations of ET.

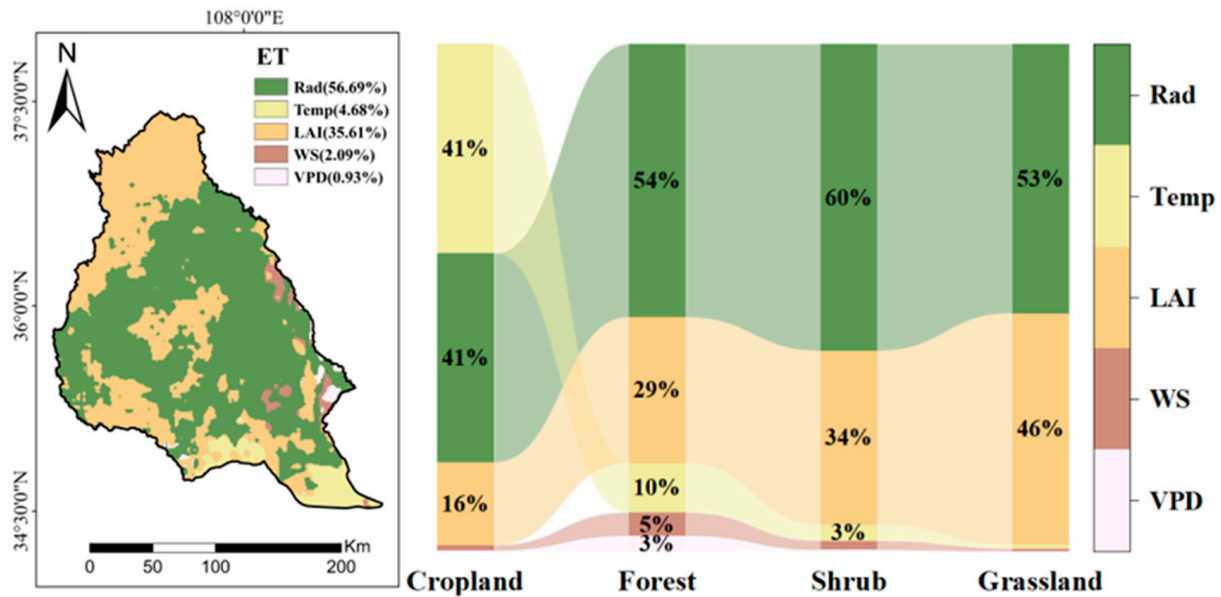


Figure 11. The geographic dispersion traits of key influencing elements on regional evapotranspiration fluctuations between 1984 and 2018.

A path analysis was performed to elucidate both direct and indirect influences of diverse drivers on evapotranspiration (ET) within the Jing River Basin, as detailed in Table 1. Findings indicated a clear direct correlation between ET and pertinent variables. The culminating structural equation model (SEM) is depicted in Figure 12. The model’s efficacy is commendable, evidenced by a Comparative Fit Index (CFI) of 0.99 and a Root Mean Square Error Approximation (RMSEA) of 0.093. Employing the chosen variables—leaf area index (LAI), radiation (Rad), temperature (Temp), precipitation (Pre), wind speed (WS), and vapor pressure deficit (VPD)—the developed SEM accounted for 96% of the variance in ET ($R^2 = 0.96$). In summary, LAI emerges as the most indicative ecological parameter reflecting shifts in ET, exerting a cumulative impact of 0.78. Additionally, VPD, PRE, and TEMP function as intermediary variables, being indirectly influenced by LAI and subsequently affecting ET to a lesser extent (0.12). Additionally, WS indirectly influences ET changes through LAI (WS → LAI → ET, WS → LAI → TEMP → ET, WS → LAI → PRE → ET) (0.051) and through RAD (WS → RAD → TEMP → ET) (0.008). Besides its direct effect on ET, RAD also indirectly influences ET changes through TEMP (RAD → TEMP → ET), with an influence coefficient of 0.027. PRE is also related to ET variations, with a total impact coefficient of 0.0883, and it indirectly influences ET changes through TEMP (PRE → TEMP → ET) (0.004). Both VPD and WS have negative direct effects on ET, with influence coefficients of -0.12 and -0.102 , respectively.

Table 1. Path coefficients of factors.

Output Item	Factors	Direct Path Coefficients	Indirect Path Coefficient						A Sum of Indirect Path	Total Path Coefficients
			LAI	Rad	Pre	Temp	VPD	WS		
ET	LAI	0.078	-	-	0.032	0.05	0.038	-	0.12	0.9
	Rad	0.042	-	-	-	0.027	-	-	0.027	0.447
	Pre	0.004	-	-	-	0.004	0.0007	-	0.0047	0.008
	Temp	0.099	-	-	-	-	-	-	-	0.099
	VPD	-0.102	-	-	-	-	-	-	-	-0.102
	WS	-0.12	0.051	-	0.008	0.027	0.082	-	0.168	0.66

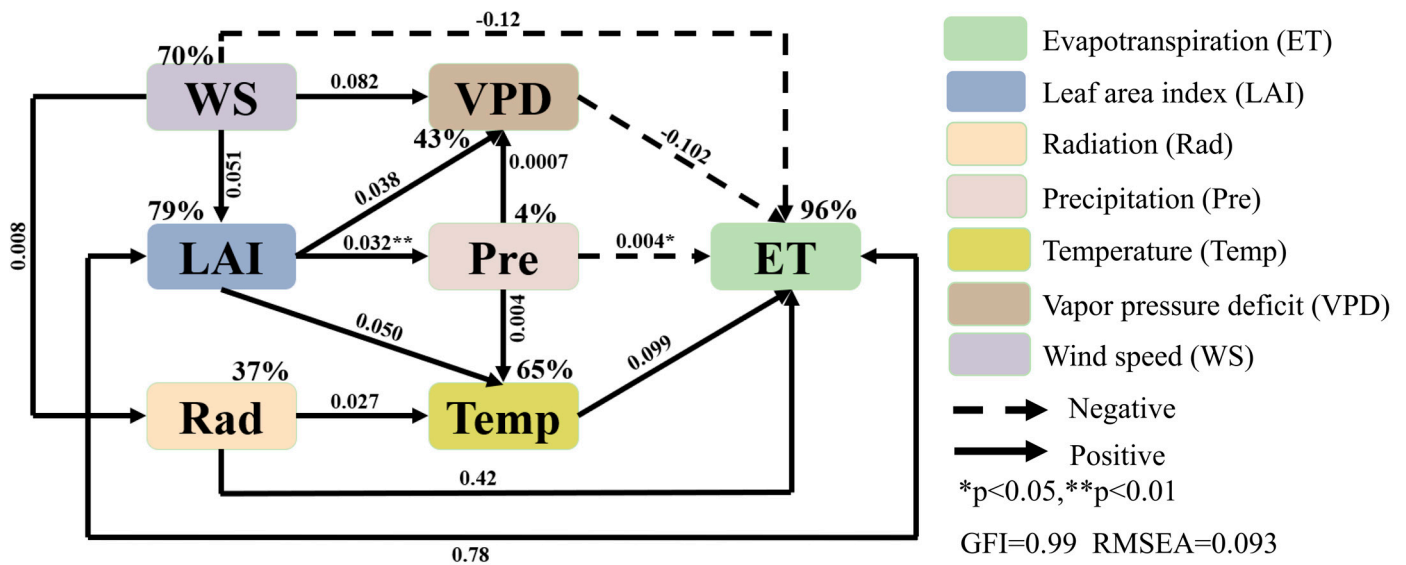


Figure 12. In the context of assessing the influence of both leaf area index and climatic factors on evapotranspiration fluctuations, a schematic representation known as the structural equation modeling (SEM) graph is employed to discern the explicit and implicit effects at play.

4. Discussion

4.1. Rate Analysis and Attribution Discussion

We analyze the impact of climatic factors on evapotranspiration (ET) in the Jing River Basin through various statistical techniques. Our results show that the mean annual ET in the region is 538 mm, with the maximum yearly ET reaching 600 mm. The highest ET recorded since 1984 occurred in 2016. This phenomenon may be related to climate factors. The changes of precipitation, temperature, vegetation quantity, and wind speed affect the evapotranspiration process through many ways, such as the supply of soil water, the physiological activities of plants, the diffusion and transportation of water vapor, etc., causing a change in the amount of evapotranspiration. Based on data from the “China Climate Bulletin” and concurrent climate records, climate change in 2017 had an impact on evapotranspiration in the Jing River Basin. Specifically, precipitation, temperature, and wind speeds were higher than historical averages that year, while relative humidity was lower. This climate condition may have led to increased evaporation rates, affecting the hydrological cycle and soil moisture conditions in the region [18,45]. Furthermore, environmental restoration policies implemented in the JRB may also contribute to these phenomena. These policies likely include vegetation recovery projects aimed at improving the ecological environment and preventing soil erosion. However, if water-consuming plant species are introduced during the vegetation reconstruction process or if local water resource carrying capacity is not adequately considered, these measures may indirectly exacerbate soil moisture depletion, affecting the variation in evapotranspiration [46,47]. The lowest ET value occurred in 1989, possibly related to the lower wind speeds and higher relative humidity in the JRB that year. High evapotranspiration (ET) values are predominantly found in regions with lower latitudes within the study area. This pattern can be linked to implementing the Grain for Green program since 2002, which has effectively enhanced vegetation coverage across numerous regions, thereby contributing positively to local ecological restoration [48]. Increased vegetation often leads to higher precipitation levels due to the improved capacity of the surface to retain and conserve water, thus facilitating the water cycle and potentially resulting in an upward trend in ET [45,47,49]. Some northern parts of the study region might experience lower evapotranspiration (ET) due to their inland position, severe weather conditions, inferior soil quality, and reduced vegetation cover. These factors can hinder plant growth and diminish the moisture transfer from the ground to the atmosphere, ultimately leading to lower overall ET rates. From

1984 to 2018, most areas in the study region exhibited an upward trend in ET, which can be attributed to both climate change and national environmental policies. The Three-North Shelterbelt Program, a significant ecological initiative by the Chinese government aimed at combating desertification and improving the ecosystem, has played a pivotal role in this region. It encompasses northwestern, northern, and northeastern China, as well as the middle reaches of the Yangtze River. It has achieved substantial ecological and social-economic benefits through actions like tree planting, afforestation, converting farmland into forests and grasslands, and controlling desertification. Additionally, the “Sealing Mountains for Reforestation” policy focuses on safeguarding and restoring forest resources, minimizing harmful human activities, and fostering natural regeneration and biodiversity recovery. Afforestation practices involve planting trees to expand forest cover, strengthen carbon absorption capabilities, and contribute to improved soil health and water conservation functions [50,51]. In the southeastern area, a notable decline in ET has been observed, attributable primarily to the expansion of the population, swift economic advancement, and the ongoing process of urban transformation, all of which contribute to a diminishing rate of vegetative cover [51].

From 1984 to 2018, the LAI increased more in the marginal areas of the study region, with the highest LAI occurring in 2018. This can be partly attributed to the afforestation ecological restoration policies [52,53]. The lowest LAI value occurred in 1997, possibly related to extensive deforestation causing vegetation destruction and soil erosion. The interannual variation rate of annual radiation was $0.41 \text{ W/m}^2/\text{year}$. This could be due to soil erosion in the Loess Plateau. The LAI directly reflects the extent and density of vegetation cover. With a rise in the leaf area index (LAI), there is an expansion in the coverage of plant life, which intensifies the process of water vapor release into the atmosphere through leaves. Consequently, this necessitates an increased uptake of water by plants from the soil to fulfill the demands associated with this enhanced evaporation process [22]. Vegetation absorbs carbon dioxide and releases water vapor, promoting gas exchange. The larger the LAI, the more that light is captured by photosynthesis and the stronger the transpiration, releasing more water into the atmosphere.

The distribution of yearly rainfall exhibits a progressive decline, moving from the north towards the southeast. On average, this region receives approximately 512 mm of precipitation. However, in certain areas, the amount can peak at around 745 mm. The increase in rainfall could be attributed to rising temperatures, which enhance plant transpiration and lead to more rainfall. The annual temperature increase rate is $0.07 \text{ }^\circ\text{C}$ per year, with the coldest year being 1984 and the warmest being 2017. This trend is probably due to rising CO_2 levels and global warming in recent decades, resulting in higher temperatures. Over the period from 1984 to 2018, changes in evapotranspiration (ET) in the Jing River Basin are closely linked to climatic factors like vegetation radiation temperature and precipitation. Temperature fluctuations had only a minor effect on ET, contributing negatively by -1.5 mm per year with a correlation coefficient of -0.33 , while radiation had a positive influence of 0.34 mm per year. According to Stefan–Boltzmann’s Law, even minor fluctuations in temperature can lead to substantial alterations in radiant flux density, and elevated surface temperatures can enhance ground radiation [54]. As plant cells respond to radiation, the radiation increases stomatal closure, reducing water loss and thus decreasing transpiration. Higher temperatures can boost plant metabolic activities and biochemical reactions, offering additional energy and resources for transpiration.

The average PCC between Rad and ET is 0.25, indicating that enhanced irradiance activates water molecules and promotes the transition from liquid to gaseous states, enhancing evaporation. However, under certain conditions, Rad suppresses ET in the surrounding areas of the Jing River Basin. Intense radiation caused by high temperatures and low relative humidity can promote evaporation rates; if evaporation exceeds the water supply, it depletes surface water and suppresses evaporation [55]. Solar radiation is the primary source of energy received by the Earth’s surface, and this energy is transmitted to the surface and atmosphere in the form of heat, which increases the surface

and atmosphere temperature, thereby increasing the kinetic energy of water molecules and promoting evaporation. In addition, solar radiation can also directly irradiate to the water surface, increase water surface temperature, accelerate evaporation rate. Furthermore, the indirect effect of radiation on evapotranspiration involves influencing evapotranspiration by changing land surface characteristics and atmospheric conditions. For example, solar radiation can change the albedo of the Earth's surface, affecting the energy it absorbs and the surface temperature and evaporation potential. Radiation can affect plant growth and alter transpiration because plants release large amounts of water into the atmosphere through transpiration. Precipitation (Pre) shows an overall negative correlation with ET, with an average PCC of -0.29 . Rainfall is a vital water resource, and increased precipitation provides more water for evaporation. Rainwater covers the land surface, moistening the soil to provide sufficient moisture for transpiration. Notably, the most significant inhibition is linked to temperature, contrary to the conventional belief that higher temperatures enhance evapotranspiration (ET). Rainfall increases, but evapotranspiration decreases. This may be because natural surface concrete and other waterproof materials cover the soil during urbanization, reducing the chance of rainwater reaching the soil and increasing temperatures as a result of the urban heat island effect. This will increase the amount of condensation in the atmosphere, which will result in less evapotranspiration as soil moisture returns to the atmosphere through transpiration due to reduced vegetation in urbanized areas. In addition, climate change can lead to changes in precipitation patterns, for example, as soil may not have enough time to absorb water due to a short period of heavy rainfall, leading to the release of water through surface runoff, instead of entering the atmosphere through evapotranspiration. Finally, changes in wind speed may accelerate the evaporation of water from the surface into the atmosphere, increasing the saturation of the air with an increase in humidity, further limiting evaporation, and vice versa. A robust negative relationship exists between temperature and ET, with a partial correlation coefficient of -0.33 , defying the common assumption that higher temperatures increase ET. In arid areas of the Loess Plateau, this finding may be due to insufficient soil moisture supply; even with temperature increases, there is not enough water available to support widespread evaporation across the surface. The correlation between relative humidity and ET is weakly negative, with an average PCC of -0.037 , and strong positive correlations in the west, reaching up to 0.47 . In contrast, strong negative correlations are observed in the southeast and east, with values of -0.48 . About vapor pressure deficit (VPD), its association with evapotranspiration (ET) exhibits a feeble and inverse relationship, characterized by an average Pearson Correlation Coefficient (PCC) of -0.037 . The contribution of VPD to ET is adversely impactful, partially because a diminished VPD impairs the water transitioning from a liquid state to a gaseous one. At reduced humidity levels, the propensity for water molecules to transform into vapor diminishes, thereby curtailing the rate of water evaporation [3]. When VPD was higher, plants would reduce transpiration rate by closing stomata to minimize water loss. The closure of stomata can reduce water loss, but it can also limit the uptake of carbon dioxide by plants and affect photosynthesis. Plants and ecosystems may develop a series of physiological and ecological strategies to cope with high VPD conditions through long-term adaptation to environmental changes, such as increasing water use efficiency and changing growth cycle, etc. These adaptive measures may result in a reduction in evapotranspiration.

In this study, Rad is the dominant factor in ET over the JRB, and there is a mutual influence between ground radiation and evapotranspiration. When the ground temperature drops, the solar radiation incident on the ground decreases, while the ground radiation increases. Part of the sunlight that reaches the Earth's surface bounces back into the atmosphere, while some gets transformed into heat energy emitted by the surface. When ground radiation increases, it will lead to increased evaporation, as high temperatures and abundant energy can cause water vapor to sublime into water vapor, increasing the moisture content in the atmosphere. At the same time, when surface radiation decreases,

evaporation will also decrease, as water vapor will be constrained by radiation energy, causing it to condense into droplets and fall, thereby reducing the moisture content in the atmosphere [15].

4.2. Effects of Human Activities and Soil Properties

The Loess Plateau, with its unique soil structure and historical overexploitation, has long been facing severe problems of soil erosion [56,57]. Soil erosion problems not only alter the terrain but also lead to numerous ecological and environmental issues. With changes in the landscape, exposed loess surfaces increase the area receiving direct solar radiation, leading to higher surface temperatures and more incredible radiative energy. In this situation, soil moisture is more easily evaporated, accelerating the consumption of soil moisture [58]. For plants growing in this region, the rapid loss of soil moisture means they find it more difficult to access water. To adapt to such arid conditions, plants may develop a range of physiological and morphological adaptive mechanisms for self-protection [59]. If soil erosion continues to worsen beyond the adaptation limits of the plants, even these resilient species may struggle to maintain average growth and reproduction, ultimately leading to vegetation degradation and a decline in ecosystem function [60,61]. Managing soil loss, improving soil conservation, and implementing evidence-based re-vegetation practices are crucial for restoring the ecology and water resources across the Loess Plateau and the wider Jing River Basin. Erosion has significantly altered the landscape, leading to a progressive reduction in altitude in some areas of the basin. Increased solar radiation accelerates water evaporation from the soil, limiting the ability of plant roots to absorb water, which in turn impacts transpiration—a mechanism of plant self-defense. Soil properties are one of the critical factors affecting regional evapotranspiration. Soil physical and chemical properties, such as soil texture, organic matter content, water holding capacity, and permeability, will directly affect soil water dynamics and plant root water supply, thus affecting the process of evapotranspiration. For example, areas with high soil moisture often have more significant potential for evapotranspiration because the soil provides more water for plant absorption and evaporation [62]. In addition, the color and structure of soil also affect its absorption and reflection of solar radiation, and they further jeopardize the soil surface temperature and water evaporation rate.

Human activities, including farming, urbanization, hydraulic engineering, and land use change, have a significant impact on regional evapotranspiration [63]. These activities can change land cover types and management practices, thus altering the water and energy balance of the land surface. For example, agricultural irrigation increases soil moisture and crop evapotranspiration; urban hardening reduces water infiltration and evaporation and alters land surface energy distribution; and ecological restoration measures such as conversion of cropland to forests may increase vegetation coverage and evapotranspiration. The effects of soil properties and human activities on evapotranspiration in an area are intertwined. The soil's initial conditions determine its capacity to retain rainfall and irrigation water, while human activities alter soil water status and evapotranspiration potential by changing soil cover and management practices. The combined effect of these factors determines the characteristics of actual evapotranspiration and time variation in a specific region. In Some Random Places, for example, evapotranspiration has risen due to improved soil water conditions and increased vegetation cover after the conversion of cropland to forests.

4.3. Implications for Water Management and Vegetation Restoration

Under the continuous advancement of key ecological projects in China, such as the sandstorm source treatment initiative in the Beijing–Tianjin region, the vast Three-North Shelterbelt System construction, and the pilot-satisfied land conservation zones, our country's ecological restoration and governance efforts have become increasingly robust [48]. The trend of land desertification has experienced a historic leap from expansion to regression [64]. Previous research results suggest that although an increase in vegetation

does intensify water uptake and transpiration, potentially exacerbating the water scarcity situation in the Loess Plateau, the response of regional water resources to vegetation changes varies. Quantitative research findings on this variability are crucial for precisely guiding vegetation layout adjustments and avoiding the risk of water shortages [65]. Consequently, adopting conservation practices for water usage and meticulously strategizing the allocation of limited water supplies to mitigate local water stress is an endeavor of significant magnitude. To achieve this, we can use a variety of management strategies to balance ecological protection with hydrological management. Indeed, strategies aimed at promoting reforestation are capable of strengthening the soil's aptitude for holding water, which in turn supports the renewal of underground aquifers and enhances the situation for individuals situated along river networks. These approaches can additionally lead to a refinement in the way current flora make use of available water supplies [66,67]. Additionally, managers need to deeply understand the local ecological context and select appropriate plant species to adjust the current vegetation composition and pattern, seeking a delicate balance between environmental and hydrological interests to optimize both environmental and water resource benefits [68–70].

The research findings suggest a hierarchy in water usage among various plant communities, with forests exhibiting the highest demand, followed by croplands, shrubs, and grasslands. These insights offer valuable guidance for optimizing vegetation composition and informing strategic ecological planning within the JRB region. Given the varying water storage potential, dynamic supply and demand balance, and evaporation characteristics of different land types, we should design targeted ecological restoration plans accordingly [71,72]. It involves selecting appropriate vegetation regeneration models, determining suitable planting ranges and plant spacing, and ensuring the scientific and practical effectiveness of ecological restoration work. In future vegetation recovery practices, we should select water-efficient and ecologically significant plant species based on their evapotranspiration characteristics and local environmental factors, using them as the cornerstone for adjusting regional vegetation layouts and enhancing their ecological functions [72].

The accessibility of water supply significantly influences the fluctuations in evapotranspiration levels among various land categories [71,72]. Therefore, in arid areas with little rainfall, it is necessary to carefully select plants with low water consumption and avoid planting plants with high water consumption in large areas. Especially in places with dense vegetation cover and vast green spaces, those plants with strong water absorption capacity should be phased out in a planned way to protect limited water resources.

4.4. Uncertainty and Limitations

There are some uncertainties in this study. First, when conducting an extensive analysis of remote sensing data, it is inevitable to encounter challenges in spatiotemporal accuracy, which stem from limitations such as spatial resolution and data quality. These inherent constraints may impact the final relevance findings [73]. In future graduate studies, remote sensing data from different sensors, which may have different spatial, spectral, or temporal resolutions, can be combined. Through the fusion, the information can be obtained from the complementary point of view to improve the overall spatial–temporal accuracy. In addition, spatial interpolation techniques in GIS such as Kriging and inverse distance weighting can be used to estimate the values of unobserved regions, thus improving the spatial resolution. Secondly, image radiation will produce errors. For example, optical cameras and photoelectric scanners mainly cause errors caused by the sensor itself. In the process of the propagation of electromagnetic waves in the atmosphere, they are affected by the action of the particles in the atmosphere, which will be reflected, refracted against, absorbed, scattered, and transmitted, which will affect the absorption of electromagnetic waves by the sensor. In addition, due to the changes in the solar altitude angle and azimuth angle, as well as the changes in the terrain undulation, different surface locations receive different solar radiation. Due to the difference in sensor characteristics, interference, and fault, the remote sensing image causes abnormal stripes and spots, which affect the

statistical calculation of the image to a certain extent. In the PT-JPL model, various sources of information are used to estimate evapotranspiration and its components, including land use types, meteorological data, and satellite imagery. To ensure consistency among these datasets, bilinear interpolation is applied to adjust their resolutions, thereby improving the spatial detail of lower-resolution remote sensing and meteorological data. However, this process might introduce extra uncertainties due to the simulation involved [74]. This error can be addressed by using multi-scale remote sensing data combined with images of different resolutions, which can take advantage of the extensive coverage and temporal continuity of low-resolution data while maintaining high-resolution details or using data fusion algorithms, such as Kalman filter or particle filtering, to integrate remote sensing and meteorological data from different sources. These methods can consider the uncertainty of data and reduce the error in the fusion process.

5. Conclusions

This study carried out a detailed spatiotemporal analysis of evapotranspiration patterns, partial correlation, multiple regression, and contribution analysis in the Jing River Basin from 1984 to 2018 using the GLASS leaf area index product. It measured the contributions of five climatic factors and vegetation to evapotranspiration and revealed the relationships between these drivers and evapotranspiration through partial correlation analysis. The main findings include as follows:

- (1) Over time, ET (Slope = 3.05 mm/year, $p < 0.01$), LAI (Slope = 0.03 m²/m²/year), Rad (0.41 W/m²/year, $p < 0.01$), Temp (0.07 °C/year), Pre (Slope = 1.94 mm/year, $p = 0.24$), VPD (Slope = 0.01 Kpa/year, $p < 0.01$), WS (Slope = 0.01 m/s/year, $p < 0.01$) showed a significant upward trend. Spatially, ET increased from the northwest (314 mm) to the southeast (736.65 mm), LAI increased from the northwest (0.25 m²/m²) to the east (4.9 m²/m²), and Rad decreased from the middle (432.19 W/m²) to the edge (490.99 W/m²). Pre increased from the southeast (296.11 mm) to the northwest (611.96 mm), Temp increased from the southeast (1.73 °C) to the northwest (15.12 °C), VPD decreased from the middle (0.45 kpa) to the edge (0.15 kpa), and WS decreased from the northwest (2.08 m/s) to the southeast (1.15 m/s).
- (2) Multi-variable analysis revealed that vegetation greening was the key driver behind the rise in evapotranspiration (ET), contributing 0.41 mm. There was also a robust positive linkage between greenery, radiation, and ET. Amongst meteorological factors, radiation played a pivotal role in enhancing ET, at a rate of 0.34 mm per annum, covering 56.69% of the study area. In agricultural lands, temperature and radiation were the principal contributors to the ET uptick. Wind speed and vapor pressure deficit (VPD) exerted some modulating influence on ET fluctuations, albeit their regulatory strength was moderate. Rainfall's impact on ET in the Jing River Basin was negligible, which consequently influenced the contributions of wind speed and relative humidity to ET within the basin.
- (3) Regarding spatial distribution, the alteration in evapotranspiration (ET) influenced by radiation predominated over half of the research region, with a focal point in the central zone of the JRB. The leaf area index (LAI) predominantly governed the ET fluctuations towards the northwest, encompassing approximately 35.61% of the investigated territory. Meanwhile, temperature, wind velocity, and relative humidity collectively shaped the ET dynamics in the southeastern part of the Jing River. These insights hold significance for aiding regional authorities in crafting effective strategies for water conservation and vegetation rehabilitation.

Author Contributions: Conceptualization and supervision: Y.L. and L.Y.; design and methodology: Z.W. (Zijun Wang), Y.L. and T.X.; data analysis: R.W., Z.W. (Zijun Wang), P.H. and L.Y.; data curation: E.H., Z.W. (Zhongming Wen), H.S. and J.Y.; writing—original draft preparation: Y.L., P.H., J.H., L.Y. and Y.Z.; writing—review and editing: L.Y. and Y.L. All authors have read and agreed to the published version of the manuscript.

Funding: This work was supported by Open Foundation of the Key Laboratory of Coupling Process and Effect of Natural Resources Elements (No. 2022KFKTC004), the Inner Mongolia Academy of Forestry Sciences Open Research Project, Hohhot 010010, China, Project No. KF2024MS04, the National Natural Science Foundation of China (No. 42107512), the Key R&D Plan of Shaanxi Province (No. 2024SF-YBXM-621), the Special Project of Science and Technology Innovation Plan of Shaanxi Academy of Forestry Sciences (No. SXLK2022–02-7 and SXLK2023–02-14), the Open Research Fund of State Key Laboratory of Simulation and Regulation of Water Cycle in River Basin, China Institute of Water Resources and Hydropower Research (Grant No. IWHR-SKL-KF202315), the Open Research Fund of Key Laboratory of Digital Earth Science, Chinese Academy of Sciences (No. 2022LDE003).

Data Availability Statement: Data will be made available on request.

Acknowledgments: We also acknowledge the data support from “Loess Plateau Science Data Center, National Earth System Science Data Sharing Infrastructure, National Science and Technology Infrastructure of China (<http://loess.geodata.cn>, accessed on 29 June 2024)”.

Conflicts of Interest: The authors declare that they have no known competing financial interests or personal relationships that could have appeared to influence the work reported in this paper.

References

1. Qu, Q.; Tsai, S.-B.; Tang, M.; Xu, C.; Dong, W. Marine Ecological Environment Management Based on Ecological Compensation Mechanisms. *Sustainability* **2016**, *8*, 1267. [CrossRef]
2. Fisher, J.B.; Melton, F.; Middleton, E.; Hain, C.; Anderson, M.; Allen, R.; McCabe, M.F.; Hook, S.; Baldocchi, D.; Townsend, P.A.; et al. The future of evapotranspiration: Global requirements for ecosystem functioning, carbon and climate feedbacks, agricultural management, and water resources. *Water Resour. Res.* **2017**, *53*, 2618–2626. [CrossRef]
3. Sun, S.L.; Liu, Y.B.; Chen, H.S.; Ju, W.M.; Xu, C.Y.; Liu, Y.; Zhou, B.T.; Zhou, Y.; Zhou, Y.L.; Yu, M. Causes for the increases in both evapotranspiration and water yield over vegetated mainland China during the last two decades. *Agric. For. Meteorol.* **2022**, *324*, 19. [CrossRef]
4. Shi, S.Y.; Wang, P.; Yu, J.J. Vegetation greening and climate change promote an increase in evapotranspiration across Siberia. *J. Hydrol.* **2022**, *610*, 12. [CrossRef]
5. Wang, Z.J.; Liu, Y.Y.; Wang, Z.Q.; Zhang, H.; Chen, X.; Wen, Z.M.; Lin, Z.Q.; Han, P.D.; Xue, T.Y. Quantifying the Spatiotemporal Changes in Evapotranspiration and Its Components Driven by Vegetation Greening and Climate Change in the Northern Foot of Yinshan Mountain. *Remote Sens.* **2024**, *16*, 357. [CrossRef]
6. Li, X.Y.; Zou, L.; Xia, J.; Dou, M.; Li, H.W.; Song, Z.H. Untangling the effects of climate change and land use/cover change on spatiotemporal variation of evapotranspiration over China. *J. Hydrol.* **2022**, *612*, 13. [CrossRef]
7. Lal, P.; Shekhar, A.; Gharun, M.; Das, N.N. Spatiotemporal evolution of global long-term patterns of soil moisture. *Sci. Total Environ.* **2023**, *867*, 10. [CrossRef]
8. Zeng, F.; Ma, M.G.; Di, D.R.; Shi, W.Y. Separating the Impacts of Climate Change and Human Activities on Runoff: A Review of Method and Application. *Water* **2020**, *12*, 2201. [CrossRef]
9. Cui, X.; Liu, S.; Wei, X. Impacts of forest changes on hydrology: A case study of large watersheds in the upper reaches of Minjiang River watershed in China. *Hydrol. Earth Syst. Sci.* **2012**, *16*, 4279–4290. [CrossRef]
10. Feng, H.H.; Zou, B.; Luo, J.H. Coverage-dependent amplifiers of vegetation change on global water cycle dynamics. *J. Hydrol.* **2017**, *550*, 220–229. [CrossRef]
11. Mueller, B.; Seneviratne, S.I.; Jimenez, C.; Corti, T.; Hirschi, M.; Balsamo, G.; Ciais, P.; Dirmeyer, P.; Fisher, J.B.; Guo, Z.; et al. Evaluation of global observations-based evapotranspiration datasets and IPCC AR4 simulations. *Geophys. Res. Lett.* **2011**, *38*, 7. [CrossRef]
12. Henderson-Sellers, A. Land-use change and climate. *Land Degrad. Rehabil.* **1994**, *5*, 107–126. [CrossRef]
13. Sheil, D.; Murdiyarso, D. How Forests Attract Rain: An Examination of a New Hypothesis. *Bioscience* **2009**, *59*, 341–347. [CrossRef]
14. Yosef, G.; Walko, R.; Avisar, R.; Tatarinov, F.; Rotenberg, E.; Yakir, D. Large-scale semi-arid afforestation can enhance precipitation and carbon sequestration potential. *Sci. Rep.* **2018**, *8*, 10. [CrossRef]
15. Tie, Q.; Hu, H.C.; Tian, F.Q.; Holbrook, N.M. Comparing different methods for determining forest evapotranspiration and its components at multiple temporal scales. *Sci. Total Environ.* **2018**, *633*, 12–29. [CrossRef]
16. Jin, Z.; Liang, W.; Yang, Y.T.; Zhang, W.B.; Yan, J.W.; Chen, X.J.; Li, S.; Mo, X.G. Separating Vegetation Greening and Climate Change Controls on Evapotranspiration trend over the Loess Plateau. *Sci. Rep.* **2017**, *7*, 15. [CrossRef]
17. Liu, Y.Y.; Lin, Z.Q.; Wang, Z.J.; Chen, X.; Han, P.D.; Wang, B.; Wang, Z.Q.; Wen, Z.M.; Shi, H.J.; Zhang, Z.X.; et al. Discriminating the impacts of vegetation greening and climate change on the changes in evapotranspiration and transpiration fraction over the Yellow River Basin. *Sci. Total Environ.* **2023**, *904*, 23. [CrossRef]
18. Fu, J.; Gong, Y.; Zheng, W.; Zou, J.; Zhang, M.; Zhang, Z.; Qin, J.; Liu, J.; Quan, B. Spatial-temporal variations of terrestrial evapotranspiration across China from 2000 to 2019. *Sci. Total Environ.* **2022**, *825*, 153951. [CrossRef]

19. Mo, X.; Liu, S.; Lin, Z.; Wang, S.; Hu, S. Trends in land surface evapotranspiration across China with remotely sensed NDVI and climatological data for 1981–2010. *Hydrol. Sci. J.* **2015**, *60*, 2163–2177. [[CrossRef](#)]
20. Ning, T.T.; Zhou, S.; Chang, F.Y.; Shen, H.; Li, Z.; Liu, W.Z. Interaction of vegetation, climate and topography on evapotranspiration modelling at different time scales within the Budyko framework. *Agric. For. Meteorol.* **2019**, *275*, 59–68. [[CrossRef](#)]
21. Omer, A.; Elagib, N.A.; Ma, Z.G.; Saleem, F.; Mohammed, A. Water scarcity in the Yellow River Basin under future climate change and human activities. *Sci. Total Environ.* **2020**, *749*, 13. [[CrossRef](#)]
22. Wang, K.C.; Dickinson, R.E. A review of global terrestrial evapotranspiration: Observation, modeling, climatology, and climatic variability. *Rev. Geophys.* **2012**, *50*, 54. [[CrossRef](#)]
23. Koc, D.L.; Can, M.E. Reference evapotranspiration estimate with missing climatic data and multiple linear regression models. *PeerJ* **2023**, *11*, 25. [[CrossRef](#)] [[PubMed](#)]
24. Xing, W.; Wang, W.; Shao, Q.; Song, L.; Cao, M. Estimation of Evapotranspiration and Its Components across China Based on a Modified Priestley–Taylor Algorithm Using Monthly Multi-Layer Soil Moisture Data. *Remote Sens.* **2021**, *13*, 3118. [[CrossRef](#)]
25. Jung, M.; Reichstein, M.; Ciais, P.; Seneviratne, S.I.; Sheffield, J.; Goulden, M.L.; Bonan, G.; Cescatti, A.; Chen, J.; de Jeu, R.; et al. Recent decline in the global land evapotranspiration trend due to limited moisture supply. *Nature* **2010**, *467*, 951–954. [[CrossRef](#)]
26. Xu, L.H.; Shi, Z.J.; Wang, Y.H.; Zhang, S.L.; Chu, X.Z.; Yu, P.T.; Xiong, W.; Zuo, H.J.; Wang, Y.N. Spatiotemporal variation and driving forces of reference evapotranspiration in Jing River Basin, northwest China. *Hydrol. Process.* **2015**, *29*, 4846–4862. [[CrossRef](#)]
27. Huang, C.L.; Yang, Q.K.; Huang, W.D. Analysis of the Spatial and Temporal Changes of NDVI and Its Driving Factors in the Wei and Jing River Basins. *Int. J. Environ. Res. Public Health* **2021**, *18*, 11863. [[CrossRef](#)] [[PubMed](#)]
28. Kang, S.; Evett, S.R.; Robinson, C.A.; Stewart, B.A.; Payne, W.A. Simulation of winter wheat evapotranspiration in Texas and Henan using three models of differing complexity. *Agric. Water Manag.* **2009**, *96*, 167–178. [[CrossRef](#)]
29. Zhao, X.E.; Fang, K.Y.; Chen, F.; Martín, H.; Roig, F.A. Reconstructed Jing River streamflow from western China: A 399-year perspective for hydrological changes in the Loess Plateau. *J. Hydrol.* **2023**, *621*, 15. [[CrossRef](#)]
30. Li, X.X.; Mao, R.C.; Song, J.X.; Gao, J.Q.; Shi, A.Y.; Xiang, W.; Sun, H.T. Response of Runoff Change to Soil and Water Conservation Measures in the Jing River Catchment of China. *Land* **2024**, *13*, 442. [[CrossRef](#)]
31. Jiang, B.; Liang, S.; Ma, H.; Zhang, X.; Xiao, Z.; Zhao, X.; Jia, K.; Yao, Y.; Jia, A. GLASS Daytime All-Wave Net Radiation Product: Algorithm Development and Preliminary Validation. *Remote Sens.* **2016**, *8*, 222. [[CrossRef](#)]
32. He, J.; Yang, K.; Tang, W.J.; Lu, H.; Qin, J.; Chen, Y.Y.; Li, X. The first high-resolution meteorological forcing dataset for land process studies over China. *Sci. Data* **2020**, *7*, 11. [[CrossRef](#)] [[PubMed](#)]
33. Yang, K.; He, J. China Meteorological Forcing Dataset (1979–2015). 2021. Available online: <https://data.tpdc.ac.cn/en/data/7a35329c-c53f-4267-aa07-e0037d913a21> (accessed on 29 June 2024).
34. Zhao, F.B.; Ma, S.; Wu, Y.P.; Qiu, L.J.; Wang, W.K.; Lian, Y.Q.; Chen, J.; Sivakumar, B. The role of climate change and vegetation greening on evapotranspiration variation in the Yellow River Basin, China. *Agric. For. Meteorol.* **2022**, *316*, 108842. [[CrossRef](#)]
35. Wang, W.; Cui, W.; Wang, X.J.; Chen, X. Evaluation of GLDAS-1 and GLDAS-2 Forcing Data and Noah Model Simulations over China at the Monthly Scale. *J. Hydrometeorol.* **2016**, *17*, 2815–2833. [[CrossRef](#)]
36. Zhang, Y.Q.; Kong, D.D.; Gan, R.; Chiew, F.H.S.; McVicar, T.R.; Zhang, Q.; Yang, Y.T. Coupled estimation of 500 m and 8-day resolution global evapotranspiration and gross primary production in 2002–2017. *Remote Sens. Environ.* **2019**, *222*, 165–182. [[CrossRef](#)]
37. Fisher, J.B.; Tu, K.P.; Baldocchi, D.D. Global estimates of the land-atmosphere water flux based on monthly AVHRR and ISLSCP-II data, validated at 16 FLUXNET sites. *Remote Sens. Environ.* **2008**, *112*, 901–919. [[CrossRef](#)]
38. Zhang, K.; Ma, J.Z.; Zhu, G.F.; Ma, T.; Han, T.; Feng, L.L. Parameter sensitivity analysis and optimization for a satellite-based evapotranspiration model across multiple sites using Moderate Resolution Imaging Spectroradiometer and flux data. *J. Geophys. Res.-Atmos.* **2017**, *122*, 230–245. [[CrossRef](#)]
39. Wang, C.C.; Zhang, K.; Jiang, J.; Liu, Q.; Wu, J.C.; Guo, C.L.; Cao, Q.; Tian, Y.C.; Zhu, Y.; Cao, W.X.; et al. Remotely assessing FIPAR of different vertical layers in field wheat. *Field Crop. Res.* **2023**, *297*, 11. [[CrossRef](#)]
40. Churkina, G.; Running, S.W.; Schloss, A.L.; Participants Potsdam, N.P.P.M.I. Comparing global models of terrestrial net primary productivity (NPP): The importance of water availability. *Glob. Chang. Biol.* **1999**, *5*, 46–55. [[CrossRef](#)]
41. Hou, E.Q.; Chen, C.R.; Luo, Y.Q.; Zhou, G.Y.; Kuang, Y.W.; Zhang, Y.G.; Heenan, M.; Lu, X.K.; Wen, D.Z. Effects of climate on soil phosphorus cycle and availability in natural terrestrial ecosystems. *Glob. Chang. Biol.* **2018**, *24*, 3344–3356. [[CrossRef](#)]
42. Adegbulu, A.O.; Kibbey, T.C.G. The Influence of Evaporation and Seasonal Effects on the Water Content in the Unsaturated Zone: A Multi-Year Laboratory Study. *Water* **2022**, *14*, 3294. [[CrossRef](#)]
43. Rosseel, Y. lavaan: An R Package for Structural Equation Modeling. *J. Stat. Softw.* **2012**, *48*, 1–36. [[CrossRef](#)]
44. Shao, R.; Zhang, B.Q.; Su, T.X.; Biao, L.; Cheng, L.Y.; Xue, Y.Y.; Yang, W.J. Estimating the Increase in Regional Evaporative Water Consumption as a Result of Vegetation Restoration Over the Loess Plateau, China. *J. Geophys. Res.-Atmos.* **2019**, *124*, 11783–11802. [[CrossRef](#)]
45. Ouyang, Z.; Zheng, H.; Xiao, Y.; Polasky, S.; Liu, J.; Xu, W.; Wang, Q.; Zhang, L.; Xiao, Y.; Rao, E.M.; et al. Improvements in ecosystem services from investments in natural capital. *Science* **2016**, *352*, 1455–1459. [[CrossRef](#)] [[PubMed](#)]
46. Song, Q.H.; Braeckvelt, E.; Zhang, Y.P.; Sha, L.Q.; Zhou, W.J.; Liu, Y.T.; Wu, C.S.; Lu, Z.Y.; Klemm, O. Evapotranspiration from a primary subtropical evergreen forest in Southwest China. *Ecophysiology* **2017**, *10*, 10. [[CrossRef](#)]

47. Lu, F.; Hu, H.F.; Sun, W.J.; Zhu, J.J.; Liu, G.B.; Zhou, W.M.; Zhang, Q.F.; Shi, P.L.; Liu, X.P.; Wu, X.; et al. Effects of national ecological restoration projects on carbon sequestration in China from 2001 to 2010. *Proc. Natl. Acad. Sci. USA* **2018**, *115*, 4039–4044. [[CrossRef](#)]
48. Deng, L.; Shangguan, Z.-p.; Li, R. Effects of the grain-for-green program on soil erosion in China. *Int. J. Sediment Res.* **2012**, *27*, 120–127. [[CrossRef](#)]
49. Zhang, Y.X.; Wang, Y.K.; Fu, B.; Dixit, A.M.; Chaudhary, S.; Wang, S. Impact of climatic factors on vegetation dynamics in the upper Yangtze River basin in China. *J. Mt. Sci.* **2020**, *17*, 1235–1250. [[CrossRef](#)]
50. Guo, N.; Degen, A.A.; Deng, B.; Shi, F.Y.; Bai, Y.F.; Zhang, T.; Long, R.J.; Shang, Z.H. Changes in vegetation parameters and soil nutrients along degradation and recovery successions on alpine grasslands of the Tibetan plateau. *Agric. Ecosyst. Environ.* **2019**, *284*, 12. [[CrossRef](#)]
51. Hu, Z.Y.; Chen, X.; Li, Y.M.; Zhou, Q.M.; Yin, G. Temporal and Spatial Variations of Soil Moisture Over Xinjiang Based on Multiple GLDAS Datasets. *Front. Earth Sci.* **2021**, *9*, 13. [[CrossRef](#)]
52. Katul, G.G.; Oren, R.; Manzoni, S.; Higgins, C.; Parlange, M.B. Evapotranspiration: A process driving mass transport and energy exchange in the soil-plant-atmosphere-climate system. *Rev. Geophys.* **2012**, *50*, 25. [[CrossRef](#)]
53. Bai, P.; Liu, X.M.; Zhang, Y.Q.; Liu, C.M. Assessing the Impacts of Vegetation Greenness Change on Evapotranspiration and Water Yield in China. *Water Resour. Res.* **2020**, *56*, 20. [[CrossRef](#)]
54. Yang, Z.S.; Zhang, Q.; Hao, X.C.; Yue, P. Changes in Evapotranspiration Over Global Semiarid Regions 1984–2013. *J. Geophys. Res.-Atmos.* **2019**, *124*, 2946–2963. [[CrossRef](#)]
55. Chattopadhyay, N.; Hulme, M. Evaporation and potential evapotranspiration in India under conditions of recent and future climate change. *Agric. For. Meteorol.* **1997**, *87*, 55–73. [[CrossRef](#)]
56. Liu, G.; Xu, W.N.; Liu, P.L.; Yang, M.Y.; Cai, C.F.; Zhang, Q.; Xia, Z.Y. Assessment of soil erosion risk on the Loess Plateau, China. *J. Food Agric. Environ.* **2012**, *10*, 1568–1571.
57. Yan, R.; Zhang, X.P.; Yan, S.J.; Chen, H. Estimating soil erosion response to land use/cover change in a catchment of the Loess Plateau, China. *Int. Soil Water Conserv. Res.* **2018**, *6*, 13–22. [[CrossRef](#)]
58. Shen, N.; Wang, Z.L.; Guo, Q.; Zhang, Q.W.; Wu, B.; Liu, J.N.; Ma, C.Y.; Delang, C.O.; Zhang, F.B. Soil detachment capacity by rill flow for five typical loess soils on the Loess Plateau of China. *Soil Tillage Res.* **2021**, *213*, 12. [[CrossRef](#)]
59. Zheng, F.L. Effect of vegetation changes on soil erosion on the Loess Plateau. *Pedosphere* **2006**, *16*, 420–427. [[CrossRef](#)]
60. Zheng, F.L. Effects of accelerated soil erosion on soil nutrient loss after deforestation on the Loess Plateau. *Pedosphere* **2005**, *15*, 707–715.
61. Yang, X.H.; Zhang, X.P.; Lv, D.; Yin, S.Q.; Zhang, M.X.; Zhu, Q.G.Z.; Yu, Q.; Liu, B.Y. Remote sensing estimation of the soil erosion cover-management factor for China's Loess Plateau. *Land Degrad. Dev.* **2020**, *31*, 1942–1955. [[CrossRef](#)]
62. Fares, A.; Bensley, A.; Bayabil, H.; Awal, R.; Fares, S.; Valenzuela, H.; Abbas, F. Carbon dioxide emission in relation with irrigation and organic amendments from a sweet corn field. *J. Environ. Sci. Health B* **2017**, *52*, 387–394. [[CrossRef](#)]
63. Hussein, E.A.; Abd El-Ghani, M.M.; Hamdy, R.S.; Shalabi, L.F. Do Anthropogenic Activities Affect Floristic Diversity and Vegetation Structure More Than Natural Soil Properties in Hyper-Arid Desert Environments? *Diversity* **2021**, *13*, 157. [[CrossRef](#)]
64. Cao, Y.P.; Xie, Z.Y.; Woodgate, W.; Ma, X.L.; Cleverly, J.; Pang, Y.J.; Qin, F.; Huete, A. Ecohydrological decoupling of water storage and vegetation attributed to China's large-scale ecological restoration programs. *J. Hydrol.* **2022**, *615*, 14. [[CrossRef](#)]
65. Dang, Z.Q.; Huang, Z.; Tian, F.P.; Liu, Y.; López-Vicente, M.; Wu, G.L. Five-year soil moisture response of typical cultivated grasslands in a semiarid area: Implications for vegetation restoration. *Land Degrad. Dev.* **2020**, *31*, 1078–1085. [[CrossRef](#)]
66. Zhang, S.L.; Yang, D.W.; Yang, Y.T.; Piao, S.L.; Yang, H.B.; Lei, H.M.; Fu, B.J. Excessive Afforestation and Soil Drying on China's Loess Plateau. *J. Geophys. Res.-Biogeosci.* **2018**, *123*, 923–935. [[CrossRef](#)]
67. Zhao, Y.L.; Wang, Y.Q.; Sun, H.; Lin, H.; Jin, Z.; He, M.N.; Yu, Y.L.; Zhou, W.J.; An, Z.S. Intensive land restoration profoundly alters the spatial and seasonal patterns of deep soil water storage at watershed scales. *Agric. Ecosyst. Environ.* **2019**, *280*, 129–141. [[CrossRef](#)]
68. Cao, S.X.; Chen, L.; Shankman, D.; Wang, C.M.; Wang, X.B.; Zhang, H. Excessive reliance on afforestation in China's arid and semi-arid regions: Lessons in ecological restoration. *Earth-Sci. Rev.* **2011**, *104*, 240–245. [[CrossRef](#)]
69. Tian, F.; Lü, Y.H.; Fu, B.J.; Zhang, L.; Zang, C.F.; Yang, Y.H.; Qiu, G.Y. Challenge of vegetation greening on water resources sustainability: Insights from a modeling-based analysis in Northwest China. *Hydrol. Process.* **2017**, *31*, 1469–1478. [[CrossRef](#)]
70. Caldwell, P.V.; Kennen, J.G.; Sun, G.; Kiang, J.E.; Butcher, J.B.; Eddy, M.C.; Hay, L.E.; LaFontaine, J.H.; Hain, E.F.; Nelson, S.A.C.; et al. A comparison of hydrologic models for ecological flows and water availability. *Ecohydrology* **2015**, *8*, 1525–1546. [[CrossRef](#)]
71. Zhang, B.Q.; AghaKouchak, A.; Yang, Y.T.; Wei, J.H.; Wang, G.Q. A water-energy balance approach for multi-category drought -assessment across globally diverse hydrological basins. *Agric. For. Meteorol.* **2019**, *264*, 247–265. [[CrossRef](#)]
72. Zhang, Z.X.; Chen, X.; Xu, C.Y.; Yuan, L.F.; Yong, B.; Yan, S.F. Evaluating the non-stationary relationship between precipitation and streamflow in nine major basins of China during the past 50 years. *J. Hydrol.* **2011**, *409*, 81–93. [[CrossRef](#)]

73. Hu, G.C.; Jia, L.; Menenti, M. Comparison of MOD16 and LSA-SAF MSG evapotranspiration products over Europe for 2011. *Remote Sens. Environ.* **2015**, *156*, 510–526. [[CrossRef](#)]
74. Yang, L.S.; Feng, Q.; Adamowski, J.F.; Alizadeh, M.R.; Yin, Z.L.; Wen, X.H.; Zhu, M. The role of climate change and vegetation greening on the variation of terrestrial evapotranspiration in northwest China's Qilian Mountains. *Sci. Total Environ.* **2021**, *759*, 13. [[CrossRef](#)]

Disclaimer/Publisher's Note: The statements, opinions and data contained in all publications are solely those of the individual author(s) and contributor(s) and not of MDPI and/or the editor(s). MDPI and/or the editor(s) disclaim responsibility for any injury to people or property resulting from any ideas, methods, instructions or products referred to in the content.